TROPOSPHERIC AND IONOSPHERIC PHASE PERTURBATIONS

AND DOPPLER FREQUENCY SHIFT EFFECTS

R84EMH003

George H. Millman

Michael C. Arabadjis

General Electric Company
Syracuse, New York 13221

DTIC
ELECTE
DEC 5   1984

D

DTIC FILE COPY

GENERAL ELECTRIC

MILITARY ELECTRONIC SYSTEMS OPERATION

TECHNICAL INFORMATION SERIES

Author G. H. Millman M. C. Arabadjis	Subject Category Tropospheric and Ionospheric Effects	No. R84EMH003
		Date August 1984

Title	TROPOSPHERIC AND IONOSPHERIC PHASE PERTURBATIONS AND DOPPLER FREQUENCY SHIFT EFFECTS		

Copies Available at MESO TIS Distribution Center Box 4840 (CSP 4-18) Syracuse, New York 13221	GE Class 1	No. of Pages
	Govt Class Unclassified	75

Summary

The temporal and spatial variations of the indices of refraction, i.e., dielectric constant, in the tropospheric and ionospheric media induce phase perturbations in radio signals propagated in an earth-space transmission system. Utilizing ionospheric phase scintillation spectral data, estimates are made of the magnitude of ionospheric integrated phase noise and phase noise density at specific frequencies.

The refraction phenomenon in the troposphere and ionosphere causes an error in the Doppler frequency shift of radio transmissions emitted from a nonstationary satellite and received on the ground. Estimates are made of the Doppler error for various atmospheric and solar-geophysical conditions and are applicable for frequencies in the VHF-UHF range and above.

Key Words:	Phase Perturbation
Doppler Frequency	Phase Scintillation
Faraday Effect	Propagation
Group Time Delay	Refractive Bending
Index of Refraction	Signal Degradation
Ionosphere	Spatial Variations
Phase Density	Temporal Variations
Phase Noise	Troposphere

Send to _____

_____

_____

GENERAL ELECTRIC COMPANY TECHNICAL INFORMATION

Within the limitations imposed by Government data export regulations and security classifications, the availability of General Electric Company technical information is regulated by the following classifications in order to safeguard proprietary information:

CLASS 1: GENERAL INFORMATION

Available to anyone on request.
Patent, legal and commercial review
required before issue.

CLASS 2: GENERAL COMPANY INFORMATION

Available to any General Electric Company
employee on request.
Available to any General Electric Subsidiary
or Licensee subject to existing agreements.
Disclosure outside General Electric Company
requires approval of originating component.

CLASS 3: LIMITED AVAILABILITY INFORMATION

Original Distribution to those individuals with
specific need for information.
Subsequent Company availability requires
originating component approval.
Disclosure outside General Electric Company
requires approval of originating component.

CLASS 4: HIGHLY RESTRICTED DISTRIBUTION

Original distribution to those individuals person-
ally responsible for the Company's interests in
the subject.
Copies serially numbered, assigned and recorded
by name.
Material content, and knowledge of existence,
restricted to copy holder.

GOVERNMENT SECURITY CLASSIFICATIONS, when required, take precedence in the handling of the material. Wherever not specifically disallowed, the General Electric classifications should also be included in order to obtain proper handling routines.

SECTION __Engineering Operation__

UNIT __Radar Systems Engineering__

MESO ACCOUNTING REFERENCE __511__

COLLABORATORS _____

APPROVED _____ TITLE Mgr. Radar Syst. Eng __ LOCATION __CSP 5-C4__

/R. Benfey

MINIMUM DISTRIBUTION - Government Unclassified Material (and Title Pages) in G.E. Classes 1, 2, or 3 will be the
following.

Copies	Title Page Only	To
0	1	Legal Section, MESO (Syracuse)
5	6	G-E Technical Data Center (Schenectady)

ADDITIONAL DISTRIBUTION (Keep at minimum within intent of assigned G.E. Class.)

COPIES	NAME	LOCATION
5 (CLASS 1 ONLY)	DEFENSE DOCUMENTATION CENTER	CAMERON STATION, ALEXANDRIA, VA. 22314
1	L. I. Chasen	P. O. Box 8555 Philadelphia, Pa., 19101

Accession For

NTIS GRA&I	X
DTIC TAB	☐
Unannounced	☐
Justification	

By_____
Distribution/
Availability Codes

Dist	Avail and/or Special
A	

TABLE OF CONTENTS

LIST OF ILLUSTRATIONS

LIST OF ILLUSTRATIONS (CONT)

GLOSSARY

AGARD	Advisory Group for Aerospace Research and Development
C	Coulomb
CCIR	International Radio Consultative Committee
CCMSAT	Communications Satellite Corp.
dB	Decibel
dBc	dB Relative to the Carrier
DNA	Defense Nuclear Agency
F	Farad
GHz	Gigahertz
Hz	Hertz
°K	Degrees Kelvin
kg	Kilogram(s)
kHz	Kilohertz
km	Kilometer(s)
LAN	Longitude of Ascending Node
m	Meter(s)
mbar	Millibar(s)
MHz	Megahertz
mrad	Milliradian(s)
NASA	National Aeronautics and Space Administration
NATO	North Atlantic Treaty Organization
NOAA	National Oceanic and Atmospheric Administration
rad	Radian(s)
RF	Radio Frequency
rms	Root-Mean-Square
sec	Second(s)
TID	Traveling Ionospheric Disturbance
UHF	Ultra-High Frequency

ACKNOWLEDGEMENTS

SECTION I

INTRODUCTION

Radio waves when propagating through the troposphere and the ionosphere undergo various types of signal degradation and perturbation due to the nonhomogeneous and turbulent characteristics of the media. Some of the propagation anomalies which prevail in both media are refractive-angular bending, group time delay (ranging effects), Doppler frequency shift effects, attenuation and amplitude, phase and angle-of-arrival scintillation. In the case of the ionosphere, there are additional anomalies, such as the rotation of the plane of polarization (Faraday effect) and dispersion effects.

The effectiveness and accuracy of electronic systems which require that the transmissions maintain phase coherence could be limited due to the presence, along the propagation path, of small-scale variations in the index of refraction in the troposphere and electron density irregularities in the ionosphere.

The irregularities responsible for the ionospheric amplitude and phase scintillation phenomena are considered to be aligned along the earth's magnetic field and are hypothesized to be cylindrical in shape. At the high latitudes, the elongation along the field line to the transverse direction is estimated to be about 5. In the equatorial region, the axial ratio could be on the order of 50 to 100.

Based on the assumption that the irregularities are field-aligned and located at 350-km altitude, the overall dimensions of the irregularities in the direction of the magnetic field lines have been deduced to be as large as 2500 km (Millman and Anderson, 1977).

The equatorial irregularity region appears to extend between ± 20° to ± 30° geomagnetic latitudes. At the high latitudes, the lower boundary of the irregularity region extends to about 57° geomagnetic latitude at night. During magnetic disturbances, the lower edge could descend beyond 50° geomagnetic latitude.

Differential phase measurements of the 150- and 400-MHz coherent frequencies radiated by the U.S. Navy Navigation Satellites (TRANSIT) have been used to determine the statistical characteristics of the phase fluctuations, induced by the ionospheric irregularities, on transionospheric propagated radio waves. The two frequency techniques for ionospheric

1-1

phase scintillation studies is utilized for the purpose of eliminating the effect of satellite motion and tropospheric contamination.

The passive monitoring of the polar-orbiting TRANSIT satellites' transmissions has been conducted at the Lincoln Laboratory (Crane, 1974) and the General Electric Company (Millman and Anderson, 1977; Millman, 1978) for the study of the ionospheric phase fluctuations. SRI International, on the other hand, has employed the differential phase data from the geostationary satellite, ATS-6, and the polar-orbiting DNA Wideband Satellite, DNA-002 (Rino et al, 1977).

Differential phase data disclose both large scale size (slow) and small-scale size (rapid) fluctuations. The former are brought about by the variations in the total electron content (integrated electron density) along the propagation path, while the latter arise from the electron density irregularities.

The power spectrum of the irregularities as observed by the amplitude and phase fluctuations can be characterized by a power-law shape. The largest scale size of the irregularities deduced from spectral data is on the order of 10-20 km (Crane, 1977).

The expected value of the standard deviation of the phase fluctuations at 400 MHz as deduced from the TRANSIT satellite data has been found to be as large as 2.0 rad for an analysis time interval of 10 sec (Millman, 1978). When the time interval is increased, the magnitude of the fluctuation statistics also increases.

Ionospheric scintillation is dependent on such parameters as geomagnetic latitude, longitude, local time, season, solar cycle and magnetic activity. A summary of amplitude scintillation characteristics is presented in Table 1-1 (CCIR, 1982). The morphological characteristics described in Table 1-1 are also applicable to the phase scintillation phenomenon since fluctuations in amplitude are always accompanied by fluctuations in phase. It is noted, however, that the converse does not apply.

At the present time, there is a sparsity of experimental measurements of phase scintillation data for characterizing the phenomenon on a global basis and in terms of the effect of solar activity (sunspot number) on such parameters as the phase scintillation magnitude, the frequency of occurrence and the spatial extent of the irregularity regions.

1-2

TABLE 1-1*

SOLAR-GEOPHYSICAL AND TEMPORAL DEPENDENCE OF IONOSPHERIC SCINTILLATION

Parameter	Latitude Region			
	Equatorial	Mid-Latitude	Auroral	Polar
Activity Level	Exhibits greatest extremes	Generally very quiet to moderately active	Generally moderately active to very active	Great intensity in high sunspot years
Diurnal	Maximum-Nighttime Minimum-Daytime	Maximum-Nighttime Sporadic-Daytime	Maximum-Nighttime Minimum-Daytime (not within Polar Cap)	Maximum-Nighttime

Seasonal	Longitudinal Dependent - peaks in equinoxes
	
	Accra, Ghana
	  Maximum-November and March
	  Minimum-Solstices
	Huancayo, Peru
	  Maximum-October through March
	  Minimum-May through July
	Kwajalein Island
	  Maximum-May
	  Minimum-November through December
		Maximum-Spring Minimum-Winter
		
		Tokyo, Japan
		  Maximum-Summer
		  Minimum-Winter
			Pattern a function of longitude sector	Maximum-Winter

Solar Cycle	Occurrence and intensity increase strongly with sunspot number	Inconclusive data	Occurrence and intensity increase strongly with sunspot number	Occurrence and intensity increase strongly with sunspot number

Magnetic Activity	Longitudinal dependent
	
	Accra, Ghana
	  Occurrence decreases with Kp
	Huancayo, Peru
	  March Equinox -
	  Occurrence decreases with Kp
	  June Solstice-
	  Occurrence increases with Kp
	  September Equinox-
	  0000-0400 Hrs (Local time)
	  Occurrence increases with Kp
		Independent of Kp	Occurrence increases with Kp	Occurrence increases moderately with Kp

*CCIR, REPORT 263-4

A considerable amount of amplitude scintillation data has been collected, utilizing satellite transmissions, by such organizations as the Air Force Geophysics Laboratory and the Communications Satellite Corp. (COMSAT) Laboratories. Amplitude scintillations have been observed in the frequency range of 20 MHz to 7 GHz with most of the data being collected at very-high frequency (VHF) (Aarons, 1982).

Because of the refractive bending encountered in the troposphere and the ionosphere, an error is introduced in the Doppler frequency shift of radio transmissions emanating from satellites and in the determination of the radial velocity of space-borne vehicles.

In this report, the phase perturbations induced by the troposphere and ionosphere on radio waves are evaluated. In addition, the characteristics of the Doppler frequency shift and the errors that can result in the reception of transmissions from satellites traversing circular-polar orbits, an elliptical-polar orbit and an orbital path of small inclination at geosynchronous altitude are presented.

SECTION II

THEORETICAL CONSIDERATIONS

2.1 PHASE EFFECTS

2.1.1 PHASE SHIFT

The phase of an RF signal received on the ground from a transmitter located on a spacecraft can be represented by

$$\phi = \omega t - \frac{2\pi}{\lambda} P_{ti} \qquad (2-1)$$

where ϕ is the phase (in rad), ω is the transmitted angular frequency, t is the time, and λ is the transmitted wavelength. The parameter, P_{ti}, is the phase-path length which is given by

$$P_{ti} = \int_{\cdot}^{s'} n_t \, ds \; + \; \int_{s'}^{s} n_i \, ds \qquad (2-2)$$

where n_t and n_i are the indices of refraction of the troposphere and ionosphere, respectively, s' is the path length from the ground to the base of the ionosphere (approximately 60-km altitude) and ds is the element of path length.

The index of refraction in the troposphere can be expressed in terms of the functions

$$N = (n_t - 1) \times 10^6 \qquad (2-3)$$

and

$$N = \frac{a}{T} \left(p + \frac{b\epsilon}{T} \right) \qquad (2-4)$$

where N is the refractivity, T is the air temperature (°K), p is the total pressure (mbar) and ϵ is the partial pressure of water vapor (mbar). According to Smith and Weintraub (1953), the constants, a and b, are 77.6°K/mbar and 4810°K, respectively.

The previous expression for the refractivity of air is independent of frequency in the 100-MHz to 30-GHz range. The first term in Equation (2-4), ap/T, applies to both optical and radio frequencies, and is often referred to as the dry term. The second term, abc/T^2, which is the wet term, is the water vapor relationship required only at radio frequencies.

The index of refraction in the ionosphere can be expressed by the relationship

$$n_i = \left[1 - \left(\frac{\omega_N}{\omega} \right)^2 \right]^{1/2} = \left[1 - \frac{N_e e^2}{\epsilon_0 m_e \omega^2} \right]^{1/2} \qquad (2-5)$$

where ω_N is the angular plasma frequency of the medium (rad/sec), N_e is the electron density (electrons/m^3), e is the electron charge (1.6×10^{-19} C), m_e is the electron mass (9.1×10^{-31} kg), ϵ_0 is the electric permittivity of free space ($10^{-9}/36\pi$ F/m) and ω ($=2\pi f$) is the angular frequency of the incident wave (rad/sec).

It is noted that the ionospheric refractive index is also a function of both the electron collision frequency and the earth's magnetic field. For frequencies on the order of 10 MHz and above, and at altitudes greater than 80 km, the effect of the collision frequency term on the index of refraction is negligible (Davies, 1965).

The refractive index, as defined by Equation (2-5), is applicable for estimating, for frequencies above about 30 MHz, the magnitude of propagation anomalies such as group time delay, angular-refractive bending, phase shift, Doppler frequency shift and pulse dispersion effects. For determining the effect of the ionosphere on linearly polarized transmission, i.e., Faraday effect, it is necessary to redefine the index of refraction in terms of magnetic field parameters (Millman, 1980).

Expanding Equation (2-5) by the binomial theorem and neglecting the higher order terms, it follows that, when substituting the resulting expression and Equation (2-2) in Equation (2-1), the total phase becomes

$$\phi = \omega t - \frac{2\pi}{\lambda} \int_0^{s'} n_t \, ds - \frac{2\pi}{\lambda} (s - s')$$

$$+ \frac{e^2}{4\pi \epsilon_0 m_e c f} \int_{s'}^{s} N_e \, ds \qquad (2-6)$$

where c is the free space velocity and f is the frequency.

The second term in this expression is the tropospheric phase shift, while the third term is the phase shift in the free space beyond the base of the ionosphere. The last term is the phase shift imposed by the ionosphere.

The ionospheric phase term in Equation (2-6) can be deduced by utilizing two harmonically related coherent signals transmitted from a satellite and detected on the ground. For this configuration, the differential phase between the two frequencies can be determined from

$$\Delta\phi = A\phi_1 - B\phi_2 \tag{2-7}$$

where ϕ_1 and ϕ_2 are the total phase shifts at frequencies, f_1 and f_2, respectively, and A and B are constants related to the transmitted frequencies, f_1 and f_2, according to

$$Af_1 = Bf_2 \tag{2-8}$$

Substituting Equations (2-7) and (2-8) in Equation (2-6), there results

$$\Delta\phi = \frac{e^2}{4\pi\epsilon_o m_e c f} \left[\frac{A^2 - B^2}{A}\right] \int_{s'}^{s} N_e \, ds \tag{2-9}$$

In the derivation of this expression, it is implied that the two transmitted frequencies travel along the same ray paths. In other words, the refraction effects in the ionosphere are assumed to be negligible. This assumption is justified, for the most part, for frequencies in the very-high frequency (VHF) range and above, except perhaps for propagation at the very-low elevation angles (Millman, 1966).

It is evident from Equations (2-6) and (2-9) that the phase shift imposed by the ionosphere at a frequency, f, can be expressed as a function of the differential phase by

$$\phi f = \frac{f_1}{f} \left[\frac{A}{B^2 - A^2}\right] \Delta\phi \tag{2-10}$$

2.1.2 PHASE FLUCTUATION

2.1.2.1 Troposphere

Although the tropospheric refractivity is generally modeled only as a function of altitude, the existence of spatial variations in the refractive index has been demonstrated by microwave refractometer measurements made in aircraft. In Florida, the fluctuations in the refractive index were found to be on the order of 25 N-units peak to peak at a constant altitude of 600 m (Weaver and Ringwalt, 1966). Observations conducted in New Zealand (Bean and Dutton, 1966) and Sweden (Wickerts, 1960) showed the variations to be ± 10 N-units at altitudes less than 300 m and about 5 N-units at 3000-m altitude, respectively.

In addition to the spatial variation, there is a temporal variation in the radio refractivity (Herbstreit and Thompson, 1955; Dean and Fannin, 1955), which is brought about by the instability and dynamic movements of the irregularities in the atmosphere. Experimental refractometer observations have indicated that approximately 90 percent of the refractivity fluctuations occur below 6-km altitude and that the fluctuations were correlated with cloud formations (Crane, 1964; Meyer, 1964).

The correlation with clouds indicated that the water vapor content was, to a large extent, responsible for the temporal randomness of the refractive index. The measurements also revealed that the greatest amount of instability occurred in the vicinity near the earth's surface and that the magnitude of the fluctuations decreased somewhat exponentially with increasing altitude to approximately 6 km. Above this level, the troposphere appeared to be spherically stratified (Crane, 1964; Meyer, 1964). From the measurements of temperature, water vapor, and radio refractivity at an altitude of 11 m in Colorado, Bean and Emmanuel (1969) have found that the temperature fluctuations contributed little to radio refractivity fluctuations which were primarily caused by variations in the water vapor density.

The nonstationary turbulent movements of the irregularities of the refractive index impact a random fluctuation in the phase of a radio signal transmitted through the medium.

The phase variations that can take place across the wavefront for a wave traversing the troposphere, according to Tatarski (1961), can be expressed by the function

$$D_{\phi}(\rho) = K C_{no}^2 \, k^2 \, Z_o \, \rho^{5/3} \tag{2-11}$$

where $D_\phi(\rho)$ is the mean-square phase variation over a distance ρ across the wavefront, Z_o is the path length through the scintillation region, $k (= 2\pi/\lambda)$ is the wave number of the radiation and C_{no}^2 is the value at the earth's surface of C_n^2 which is a parameter related to the structure constant of the refractive index.

The constant K is equal to 2.91 for the case in which C_n^2 decreases exponentially with the altitude Z in the form

$$C_n^2 = C_{no}^2 \exp\left[-\frac{Z}{Z_o}\right] \tag{2-12}$$

and K is equal to 4.57 for the model

$$C_n^2 = C_{no}^2 \left[1 + \left(\frac{Z}{Z_o}\right)^2\right]^{-1} \tag{2-13}$$

Lane (1968) has deduced from experimental data the values of C_{no}^2 and Z_o to be 5×10^{-14} cm$^{-2/3}$ and 2 km, respectively.

In the study of the effects of inhomogeneities in the troposphere, Muchmore and Wheelon (1955), using a ray theory approach, developed an expression for the root-mean-square (rms) phase shift, σ_ϕ, in a single ray which is of the form

$$\sigma_\phi = \left[2 L \ell \, \overline{\Delta N^2}\right]^{1/2} \frac{2\pi \times 10^{-6}}{\lambda} \tag{2-14}$$

where σ_ϕ is in radians, L is the path length through the turbulent medium, ℓ is the scale length of the turbulent eddy, $\overline{\Delta N^2}$ is the mean-square fluctuation in the refractivity N and λ is the transmitted wavelength.

This relationship, which was derived on the assumption of an exponential space correlation for the scale of turbulence, is applicable for a point antenna. The rms phase shift for a finite antenna aperture is given by

$$\sigma_\alpha = \sigma_\phi \left[1 - \frac{r^2}{\ell^2} + \cdots\cdots\right]^{1/2} \tag{2-15}$$

where r is the radius of the antenna.

2-5

The path length L, depicted in Figure 2-1, can be expressed in terms of the function

$$L = \left[h^2 + 2 r_o h + \left(r_o \sin E \right)^2 \right]^{1/2} - r_o \sin E \qquad (2\text{-}16)$$

where r_o is the radius of the earth, h is the height above the earth's surface within which the turbulent medium is contained and E is the propagation elevation angle.

In estimating the magnitude of σ_ϕ, as defined by Equation (2-6), it is assumed that the values of ΔN^2 and ℓ are such that $5 \text{ m} \leq \ell \, \Delta N^2 \leq 500 \text{ m}$ and that the turbulent medium is assumed to be located in the height interval of 5 km.

As shown in Figure 2-2, the rms phase jitter at near vertical incidence at 10 GHz could vary between approximately 2.5° and 25° and increases by a factor of about 7 for propagation along the horizon. These estimates are in agreement with the radio phase measurements taken simultaneously over the same 6-km path by Herbstreit and Thompson (1955) at a frequency of 1040 MHz and by Dean and Fannin (1955) at a frequency of 9350 MHz which yielded rms phase variations of 1.09° and 12.6°, respectively.

2.1.2.2 Ionosphere

The phase fluctuations induced by the ionosphere are the result of irregularities of electron density along the propagation path.

The mean-square phase fluctuation in the ionosphere, as derived by Booker (1958), is given by the relationship

$$\overline{\Delta\phi^2} = \frac{\ell \, L \, \omega_N^4}{4 \, c^2 \, \omega^2} \overline{\left[\frac{\Delta N_e}{N_e} \right]^2} \qquad (2\text{-}17)$$

where $\overline{\left(\Delta N_e / N_e \right)^2}$ is the mean-square fractional deviation of the electron density from the average and L and ℓ have the same definitions as in the troposphere [Equation (2-14)].

It is seen that the rms ionospheric phase fluctuation is inversely proportional to frequency while, for the troposphere as given by Equation (2-14), it is directly related.
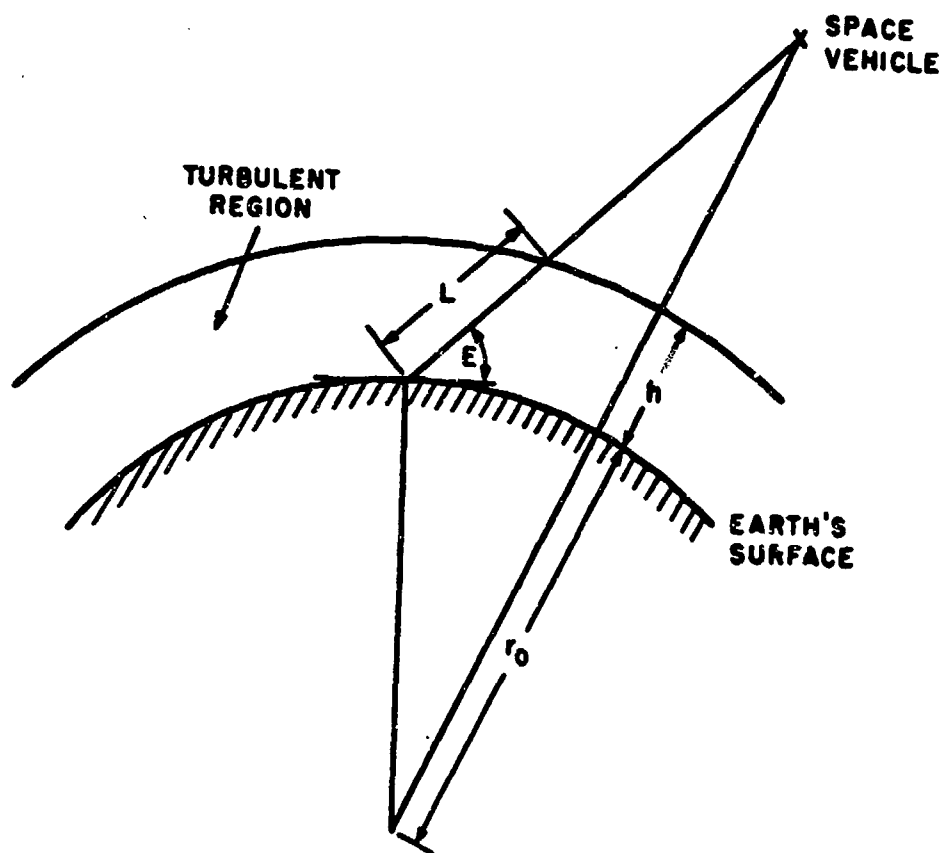
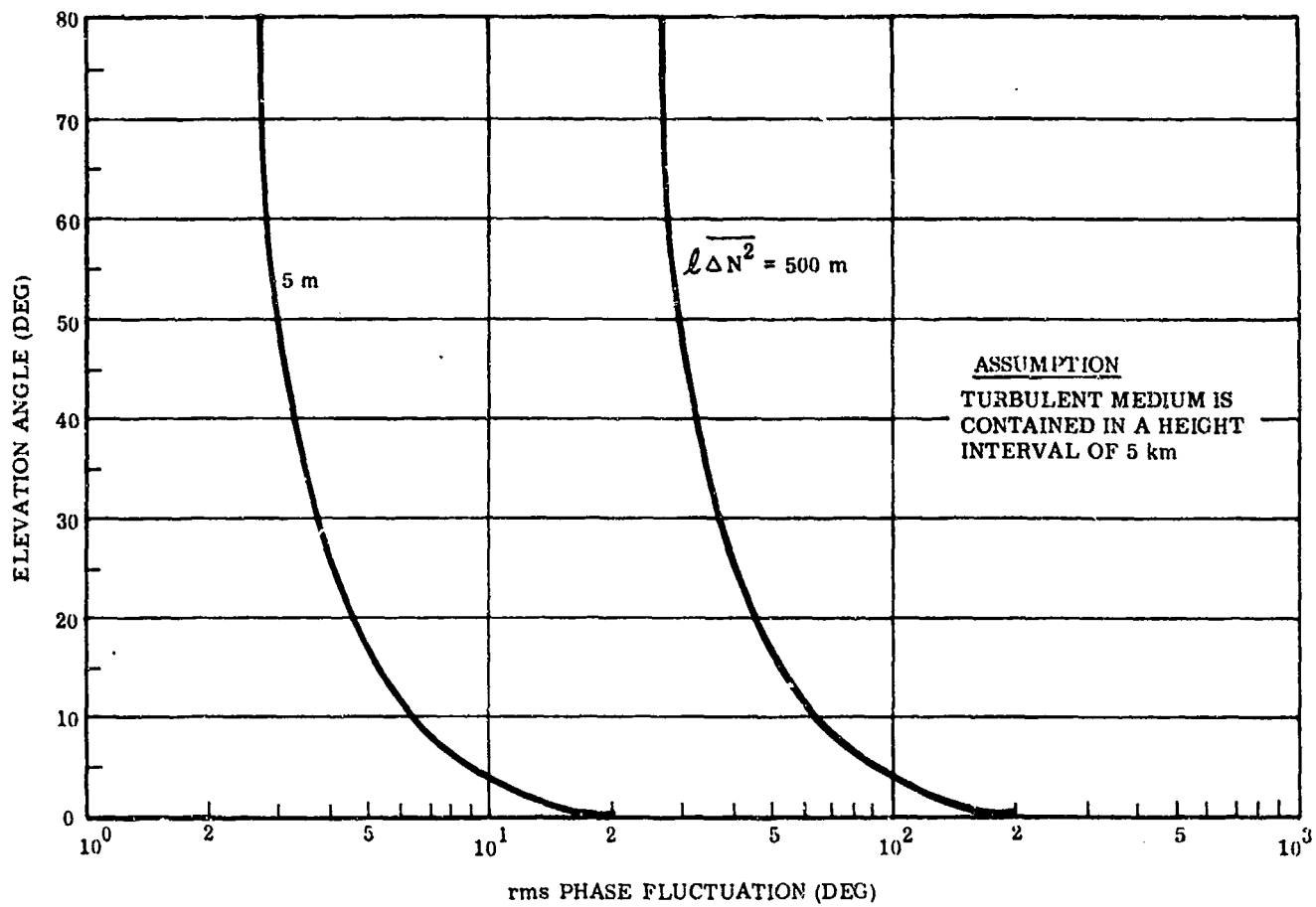Figure 2-1. Geometry for Propagation Through a Turbulent Region

Figure 2-2. Root–Mean–Square Tropospheric Phase Fluctuation at 10 GHz, One–Way Transmission Path

The ratio of $(\omega_N/\omega) = 10^{-3}$ and 5×10^{-4}, indicated in the calculations of Figure 2-3, implies a plasma frequency of 10 and 5 MHz, respectively, for a transmission frequency of 10 GHz. Assuming $\ell \left(\Delta N_e / N_e\right)^2 = 10^{-4}$ km, $(\omega_N/\omega) = 10^{-3}$ and a turbulent path length of 100 km, the rms ionospheric phase fluctuation evaluates to 0.6° at a frequency of 10 GHz, which is an order of magnitude less than the corresponding tropospheric estimate.

2.2 DOPPLER EFFECTS

2.2.1 DOPPLER SHIFT

The frequency of a radio signal emitted from a transmitter on a space vehicle, and received on the earth experiences an apparent shift. The phenomenon which is referred to as the Doppler effect occurs because of the relative motion between the source of transmission and the stationary receiver terminal.

The Doppler effect can be expressed by the relationship

$$f_d = -\frac{f}{c} \, V \cos \psi \qquad (2-18)$$

where f_d is the frequency difference between the apparent reflected frequency, f', and the transmitted frequency, f, c is the free space velocity and V is the satellite velocity. As shown in Figure 2-4, ψ is the angle between the satellite velocity vector and the direct path (i.e., line-of-sight direction).

2.2.2 DOPPLER SHIFT ERROR

Electromagnetic waves when transmitted through a medium, such as the troposphere or the ionosphere, whose dielectric constant or index of refraction is a varying function of the path, undergo a change in the direction of propagation or refractive bending. Because of the refraction phenomenon, an error is introduced in the Doppler frequency shift of radio transmissions between the earth and space vehicles. The error results from the fact that the direction of the refracted ray at the spacecraft differs slightly from the unrefracted line-of-sight direction.
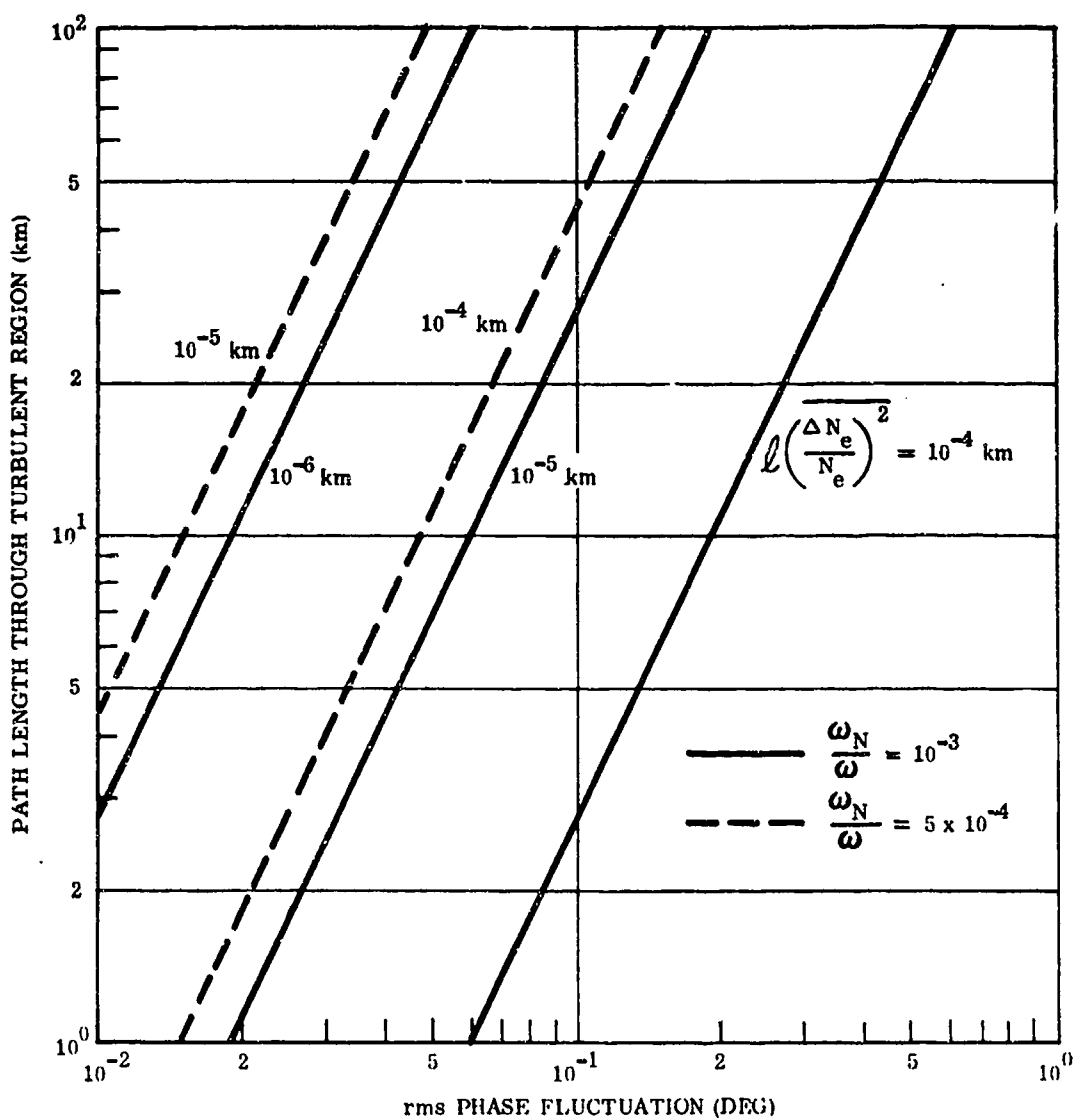
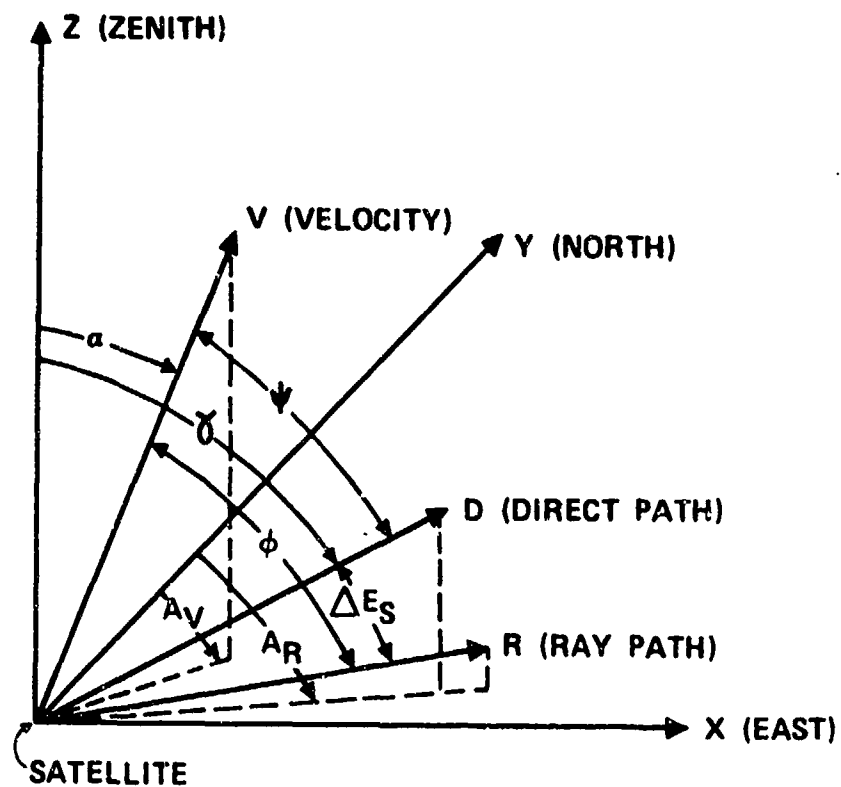Figure 2-3. Root-Mean-Square Ionospheric Phase Fluctuation at 10 GHz, One-Way Path Transmission

Figure 2-4. Satellite Velocity Geometry

The error in the Doppler frequency difference is given by

$$\Delta f_d = -\frac{f}{c} \Delta V \cos \psi \qquad (2\text{-}19)$$

where it is assumed that f and ψ are errorless quantities.

The term, $\Delta V \cos \psi$, is the component of the satellite velocity error in the direction of the line-of-sight path. According to Figure 2-4, this term is given by

$$\Delta V \cos \psi = V_D - V_R \qquad (2\text{-}20)$$

where

$$V_D = V \cos \psi \qquad (2\text{-}21)$$

$$V_R = V \cos \phi \qquad (2\text{-}22)$$

and where ϕ is the angle between the velocity vector and the ray path. It is noted that V_D and V_R are the components of the satellite velocity projected along the direct path and the ray path, respectively.

It follows from Equations (2-20) through (2-22) that Equation (2-19) can be written as

$$\Delta f_d = -\frac{f}{c} V \left[\cos \psi - \cos \phi\right] \qquad (2\text{-}23)$$

Expressions for the angles ψ and ϕ can be derived utilizing the vector analysis approach. It is assumed that the velocity, V, and the directions D (direct path) and R (ray path) are unit vectors. Thus the scalar product of the vectors $\vec{V}$ and $\vec{D}$ and $\vec{V}$ and $\vec{R}$ are

$$\vec{V} \cdot \vec{D} = |V| \, |D| \cos \psi = \cos \psi \qquad (2\text{-}24)$$

$$\vec{V} \cdot \vec{R} = |V| \, |R| \cos \phi = \cos \phi \qquad (2\text{-}25)$$

According to Figure 2-4, the vectors, $\vec{V}$, $\vec{D}$ and $\vec{R}$ can be represented by the unit vectors (i, j, k) along the X (east), Y (north) and Z (zenith) axes

$$\vec{V} = i \sin a \sin A_V + j \sin a \cos A_V + k \cos a \qquad (2\text{-}26)$$

$$\vec{D} = i \sin \gamma \sin A_R + j \sin \gamma \cos A_R + k \cos \gamma \qquad (2\text{-}27)$$

$$\vec{R} = i \sin \left(\gamma + \Delta E_s\right) \sin A_R + j \sin \left(\gamma + \Delta E_s\right) \cos A_R + k \cos \gamma \qquad (2\text{-}28)$$

It is noted that $\vec{D}$ is in the $Z - \vec{R}$ plane and that α is the angle between the Z-axis and $\vec{V}$, A_V is the azimuth angle of $\vec{V}$ measured from geographic north at the satellite location, A_R is the azimuth angle of $\vec{R}$ measured from geographic north at the satellite location, γ is the angle between the Z-axis and $\vec{D}$ and ΔE_s is the angle between $\vec{D}$ and $\vec{R}$.

Substituting Equations (2-26) and (2-27) in Equation (2-24) yields

$$\cos \psi = \sin a \sin A_V \sin \gamma \sin A_R + \sin a \cos A_V \sin \gamma \cos A_R$$
$$+ \cos a \cos \gamma \qquad (2\text{-}29)$$

Similarly, when substituting Equations (2-26) and (2-28) in Equation (2-25), it follows that

$$\cos \phi = \sin a \sin A_V \sin (\gamma + \Delta E_s) \sin A_R + \sin a \cos A_V \sin (\gamma + \Delta E_s) \cos A_R$$
$$+ \cos a \cos (\gamma + \Delta E_s) \qquad (2\text{-}30)$$

For the two-dimensional case in which $A_R = A_V = 0°$, 90°, 180° or 270°, Equations (2-29) and (2-30) simplify to

$$\cos \psi = \cos (\gamma - a) \qquad (2\text{-}31)$$

$$\cos \phi = \cos \left[(\gamma + \Delta E_s) - a\right] \qquad (2\text{-}32)$$

2-13

When substituting Equations (2-29) and (2-30) in Equation (2-23), the Doppler frequency difference error becomes

$$\Delta f_d = -\frac{f}{c} V \left\{ \sin \alpha \left[\sin \gamma - \sin \left(\gamma + \Delta E_s \right) \right] \cos \left(A_R - A_V \right) \right.$$

$$\left. + \cos \alpha \left[\cos \gamma - \cos \left(\gamma + \Delta E_s \right) \right] \right\} \tag{2-33}$$

An expression for the angles, ΔE_s and γ, can be readily derived from Figure 2-5 which illustrates the angular deviation of a ray due to the refractive effects of the medium.

It can be shown utilizing Snell's Law for spherically stratified surfaces and the law of sines that

$$\Delta E_s = \cos^{-1} \left[\frac{r_0}{r_0 + h_s} \cos \left(E_0 - \Delta E \right) \right] - \cos^{-1} \left[\frac{n_0 r_0}{n_s (r_0 + h_s)} \cos E_0 \right] \tag{2-34}$$

where n_0 and n_s are the refractive indices at the ground and space vehicle, respectively, r_0 is the radius of the earth (6371 km) and ΔE is the refraction angle error corresponding to the apparent elevation angle, E_0, and satellite altitude, h_s.

The angle, γ, is derivable from the law of the sines and is given by

$$\gamma = \sin^{-1} \left[\frac{r_0}{r_0 + h_s} \cos \left(E_0 - \Delta E \right) \right] \tag{2-35}$$

In determining an expression for the angle α, it is necessary to consider the orientation of the satellite's velocity vector with respect to the zenith as indicated in Figure 2-6. It can be shown from simple trigonometric considerations that

$$\alpha = \tan^{-1} \left\{ \frac{\sin \theta}{\cos \theta - \dfrac{r_0 + h_{s1}}{r_0 + h_{s2}}} \right\} \tag{2-36}$$
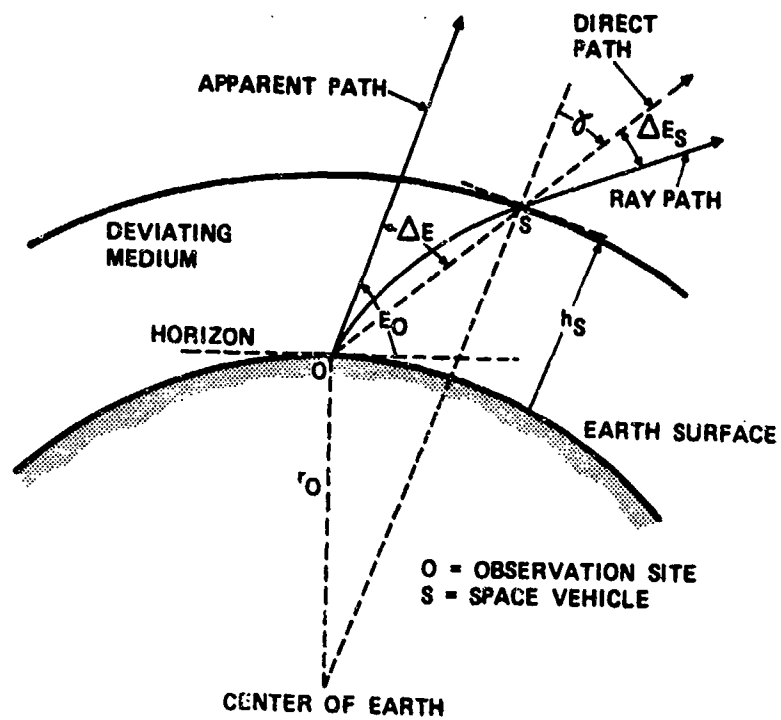
2-14

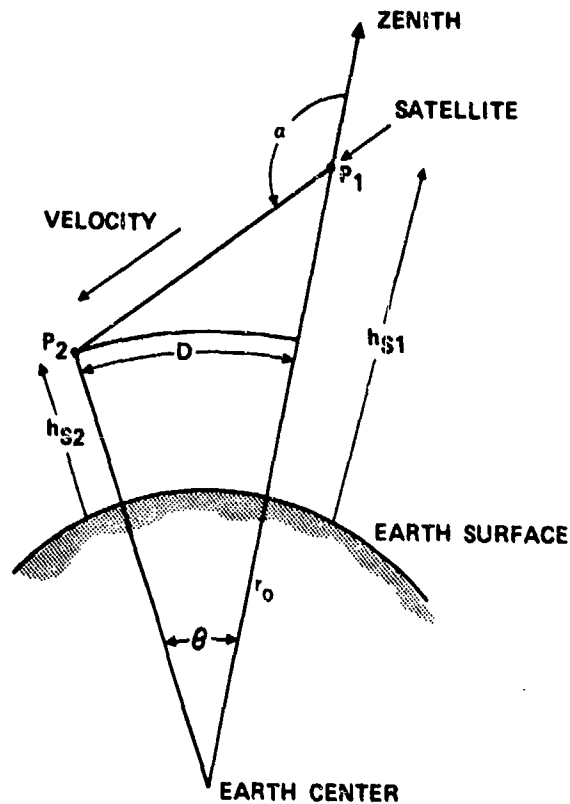Figure 2-5. Deviation of Ray Path at Space Vehicle Position

Figure 2-6. Orientation of Satellite Velocity Vector with Respect to the Zenith

where θ is the earth's central angle measured between the two satellite positions, P_1 and P_2. The parameters, h_{s1} and h_{s2}, are the altitudes of the satellite at P_1 and P_2, respectively.

For small angle θ, Equation (2-36) simplifies to

$$\alpha = \tan^{-1} \left\{ \frac{D}{h_{s2} - h_{s1}} \right\} \tag{2-37}$$

where D is the distance travelled by the satellite as projected onto the minimum altitude.

It is noted that

$$90° < \alpha \le 180° \text{ for } h_{s1} > h_{s2}$$
$$\alpha = 90° \text{ for } h_{s1} = h_{s2}$$
$$0° \le \alpha < 90° \text{ for } h_{s1} < h_{s2}$$

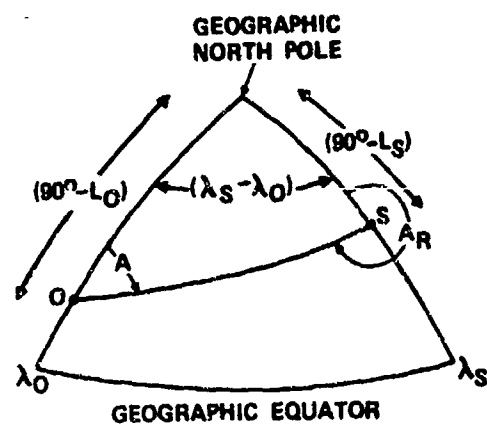The $h_{s1} = h_{s2}$ condition occurs for a satellite in a circular orbit.

The angle, A_R, which is the bearing angle of the propagation direction, i.e. ray path, at the satellite is given in Figure 2-7 which depicts the satellite geometry projected on the earth's surface. It can be readily shown from spherical trigonometry that

$$A_R = \cos^{-1} \left\{ - \cos A \cos \left(\lambda_s - \lambda_o \right) + \sin A \sin \left(\lambda_s - \lambda_o \right) \sin L_o \right\} \tag{2-38}$$

where A is the bearing of the satellite (with respect to geographic north) as measured at the observation site, L_o is the latitude of the observation site, and λ_s and λ_o are the longitudes of the satellite and observation site, respectively.
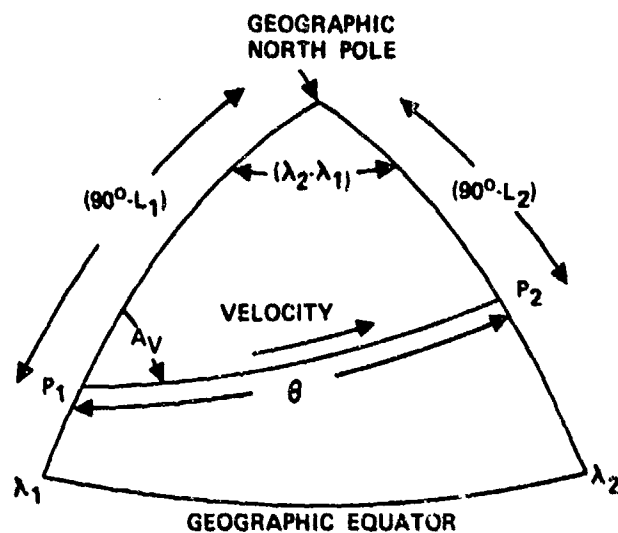
Figure 2-8 displays the bearing of the satellite orbital velocity vector, A_V, as projected on the earth's surface. It should be evident that A_V can be expressed by the function

$$A_V = \cos^{-1} \left\{ \frac{\sin L_2 - \cos \theta \sin L_1}{\sin \theta \cos L_1} \right\} \tag{2-39}$$

GEOGRAPHIC NORTH POLE

$(90^o - L_O)$ $(\lambda_S - \lambda_O)$ $(90^o - L_S)$

A

S A_R

O

λ_O λ_S

GEOGRAPHIC EQUATOR

O = OBSERVATION SITE   S = SATELLITE

L_O = OBSERVATION SITE LATITUDE L_S = SATELLITE LATITUDE

λ_O = OBSERVATION SITE LONGITUDE λ_S = SATELLITE LONGITUDE

Figure 2-7. Satellite and Observation Site Geometry

GEOGRAPHIC NORTH POLE

$(90^o - L_1)$ $(\lambda_2 - \lambda_1)$ $(90^o - L_2)$

P_2

VELOCITY

A_V

P_1

θ

λ_1 λ_2

GEOGRAPHIC EQUATOR

P_1 = SATELLITE LOCATION AT TIME t_1 P_2 = SATELLITE LOCATION AT TIME t_2

L_1 = P_1 LATITUDE L_2 = P_2 LATITUDE

λ_1 = P_1 LONGITUDE λ_2 = P_2 LONGITUDE

Figure 2-8. Bearing of the Satellite Orbital Velocity Vector

where L_1 and L_2 are the latitudes of the satellite at times t_1, and t_2, respectively. The parameter θ, the earth central angle, is given by

$$\theta = \cos^{-1} \left\{ \sin L_1 \sin L_2 + \cos L_1 \cos L_2 \cos \left(\lambda_2 - \lambda_1 \right) \right\} \tag{2-40}$$

where λ_1 and λ_2 are the longitudes of the satellite at times t_1 and t_2, respectively. It is noted that the angle θ in Equations (2-39) and (2-40) is identical to that in Equation (2-36).

2.2.2.1 Troposphere

As indicated in Equation (2-34), the angle, ΔE_s, is a function of n_o, the refractive index at the earth's surface and ΔE, the angular deviation, i.e., the elevation angle error.

The tropospheric angular deviations used in the ΔE_s estimation were determined by the statified layer method (Millman, 1958). The basic assumption which this mathematical approach embodies is that the atmosphere is considered to be stratified into spherical layers with a constant refractive index in each layer. Since the refractive index, defined by Equations (2-3) and (2-4), is independent of frequency, the tropospheric elevation angle errors are also frequency independent.

The index of refraction model used in the computations was the CRPL Reference Refractivity Atmosphere - 1958. As described by Bean and Dutton (1966), the refractivity model is given by

$$N(h) = N_0 + \left(h - h_o \right) \Delta N \tag{2-41}$$

where N_0 is the surface refractivity and h_o is surface height above mean-sea-level. This expression is valid for $h_o \leq h \leq (h_o + 1)$ km. The parameter, ΔN, is defined by

$$\Delta N = -7.32 \exp \left(0.005577 \, N_o \right) \tag{2-42}$$

For the region defined by $(h_o + 1) \leq h \leq 9$ km, the refractivity decays as

$$N(h) = N_1 \exp \left[- c \left(h - h_o - 1 \right) \right] \tag{2-43}$$

where N_1 is the value of N at 1 km above the surface and

$$C = \frac{1}{8 - h_o} \log_e \left(\frac{N_1}{105} \right) \tag{2-44}$$

Above 9-km altitude, the exponential decay is of the form

$$N(h) = 105 \exp \left[-0.1424 \, (h-9) \right] \tag{2-45}$$

It is seen that, at an altitude of 30 km, the refractivity decreases to a value of approximately 5 N-units.

2.2.2.2 Ionosphere

The ΔE_s term, specified in Equation (2-34), is also a function of the index of refraction at the satellite altitude, in addition to the elevation angle error introduced by the ionosphere.

According to Equation (2-5), the index of refraction in the ionosphere is, to a first approximation, directly proportional to the electron density and inversely proportional to the frequency squared.

The electron density at the peak of the F2 layer which is generally at an altitude on the order of 300-350 km, could attain a value as high as 3×10^{12} electrons/m^3. For this condition, the index of refraction at 100 MHz evaluates to 0.9987. The ionosphere refractive index tends toward unity as the electron density decreases and as the frequency increases. In other words, it is valid to assume that, above 100 MHz, the index of refraction at the satellite altitude can be neglected in the ΔE_s computations.

The elevation angle error imposed by the ionosphere can be expressed in terms of the range error, ΔR, by the function (Millman and Reinsmith, 1974)

$$\Delta E = \frac{\left(R + r_o \sin E_o \right) r_o \cos E_o}{\left[h_i \left(2 \, r_o + h_i \right) + \left(r_o \sin E_o \right)^2 \right]} \, \frac{\Delta R}{R} \tag{2-46}$$

2-19

where R is the range to the satellite, r_o is the radius of the earth, E_o is the apparent elevation angle of the satellite and h_i is the altitude at which the median electron content, i.e., integrated electron density, along the ray path occurs. The altitude applicable to h_i is, for the most part, between approximately 300 and 450 km. For the calculations presented in this report, a value of 400 km is assumed for h_i.

For high elevation angles, i.e., $r_o \sin E_o > R$, the angular error simplifies to

$$\Delta E = \cot E_o \frac{\Delta R}{R} \qquad (2\text{-}47)$$

For low elevation angles and long ranges, i.e., $R > r_o \sin E_o$, Equation (2-46) reduces to

$$\Delta E = \frac{\cos E_o}{2 h_i} \Delta R \qquad (2\text{-}48)$$

The range error, i.e., the increase in path length, due to the ionosphere can be defined by (Millman, 1980)

$$\Delta R = \frac{e^2}{8 \pi^2 \epsilon_o m_e f^2} \int_0^s N_e \, ds = \frac{e^2}{8 \pi^2 \epsilon_o m_e f^2} \overline{\sec \gamma} \; N_t \qquad (2\text{-}49)$$

where ds is the differential distance along the transmission path, N_t is the electron content, i.e the integrated electron density in a vertical column up to the satellite altitude, and γ is the angle between the ray path and the zenith.

The parameter, $\sec \gamma$, which is the obliquity factor accounting for the slant path geometry, is given by

$$\sec \gamma = \frac{r_o + h}{\left\{ (r_o + h)^2 - \left[r_o \cos \left(E_o - \Delta E \right) \right]^2 \right\}^{1/2}} \qquad (2\text{-}50)$$

It is noted that the angle γ in this expression is similar to that defined by Equation (2-35). In evaluating Equations (2-49) and (2-50), an average value for $\sec \gamma$ is assumed where h = 400 km and $\Delta E = 0$.

An examination of Equations (2-46) and (2-49) reveals that the ionospheric refraction-elevation angle errors are directly proportional to the electron content and inversely proportional to the frequency squared.

The presence of the ionosphere, in addition to imposing an error in the Doppler frequency shift by virtue of the refractive bending of the ray path, introduces a perturbation in the observed frequency. Since the frequency of a wave is related to the time derivative of the phase or phase path length, it can be readily shown that the nonrelativistic Doppler frequency shift, f_d, in the ionosphere can be described by the relationship (Millman, 1980)

$$f_d = -\frac{f}{c}\frac{ds}{dt} + \frac{e^2}{8\pi^2 c\,\epsilon_o\,m_e\,f}\ \frac{d}{dt}\int_0^s N_e\ ds \tag{2-51}$$

The first term in Equation (2-51) describes the Doppler frequency shift for an object moving in free space and is identical to Equation (2-18). The second term basically defines the frequency shift imposed by the ionosphere. It is seen that the Doppler shift is a function of the time derivative of the electron content along the propagation path to the object and is inversely proportional to the frequency.

SECTION III

DISCUSSION

3.1 PHASE EFFECTS

3.1.1 INTEGRATED PHASE NOISE

The ionospheric phase scintillation data employed in this study are extracted from the publications of Quinn (1980), Fremouw et al. (1978) and Gjeldum (1978). The Quinn and Fremouw data were collected in the DNA Wideband Satellite experiment, which was sponsored by the Defense Nuclear Agency. The data used by Gjeldum were collected in the ATS-6 Radio Beacon Satellite experiment, which was sponsored jointly by the National Aeronautics and Space Administration (NASA) and the National Oceanic and Atmospheric Administration (NOAA).

The DNA Wideband Satellite was launched in May 1976, in a near circular, polar orbit at an altitude of approximately 1000 km. The satellite transmitted 10 coherent frequencies ranging between 137.6748 and 2891.117 MHz and all harmonics of 11.4729 MHz. Phase data were recorded by SRI International at Ancon, Peru (11.78°S, 77.15°W), Kwajalein, Marshall Islands (9.40°N, 167.47°E), Poker Flat, Alaska (65.13°N, 147.49°W), and Stanford, California (37.40°N, 122.17°W) (Quinn, 1980; Fremouw et al., 1978).

The ATS-6 Radio Beacon Satellite was launched in May 1974 for positioning at the geosynchronous altitude (35790 km) at the geographic coordinates of approximately 0°N, 94°W. The satellite transmitted linearly polarized coherent signals at nominal carrier frequencies of 40, 140 and 360 MHz, which were all harmonics of 20.008 MHz. The phase data were recorded by NOAA at Boulder, Colorado (40.13°N, 105.24°W) (Gjeldum, 1978).

Average values of the standard deviation of the phase scintillation derived by Quinn (1980) from data acquired at Ancon, Kwajalein, Poker Flat and Stanford are depicted in Figure 3-1.

It is evident that the frequency variation is of the form, f^{-n}. The exponent, n, derived from the data in Figure 3-1 is presented in Table 3-1, together with the phase scintillation-standard deviation extrapolated to a frequency of 1 and 10 GHz. It is apparent that the standard deviation is a minimum for the phase data collected at Stanford.
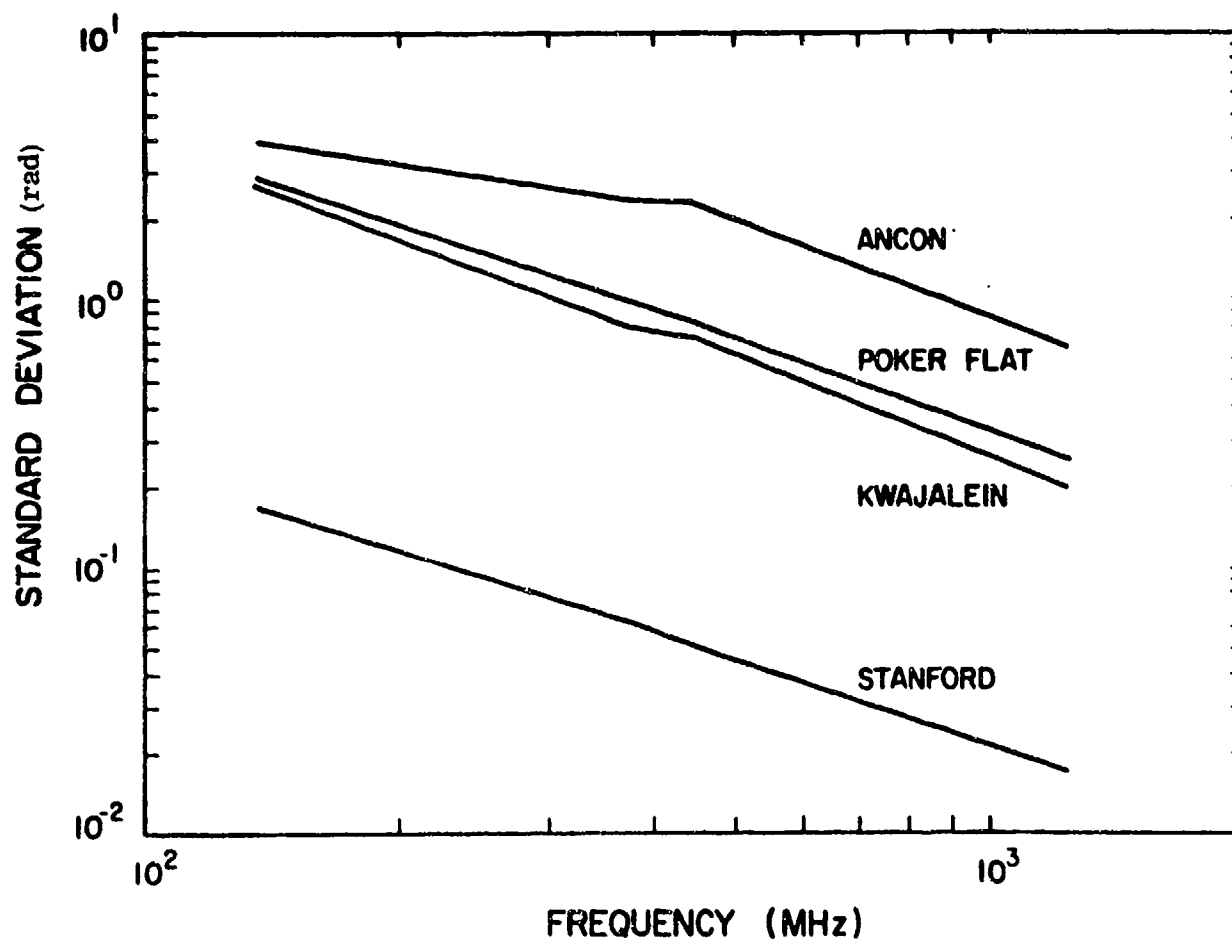
Figure 3-1. Ionospheric Phase Scintillation (After Quinn, 1980)

TABLE 3-1
STANDARD DEVIATION OF IONOSPHERIC PHASE SCINTILLATION

Observation Site	Frequency Exponent* (n)	Standard Deviation (Deg)	
		1 GHz	10 GHz
Ancon, Peru	1.201	49.849	3.138
Kwajalein, Marshall Islands	1.207	15.124	0.939
Poker Flat, Alaska	1.084	19.475	1.605
Stanford, California	1.109	1.208	0.094

*For frequency $\geq$ 500 MHz

Table 3-2 contains estimates of the integrated ionospheric phase noise deduced from the scintillation data illustrated in Appendix A. In the process of integrating the phase between 1 Hz and 20 MHz and between 10 Hz and 5 MHz, it was assumed that the last data point of the phase-power spectrum remained constant out to a frequency of 20 MHz.

An examination of Table 3-2 reveals that the standard deviation of the phase noise integrated between 10 Hz and 5 MHz, referred to 100 MHz, (1) varies between 0.037° and 7.651° and (2) is equal to approximately one-half of the 1 Hz-20 MHz value.

The effect of the latitude of the observation site on the integrated phase noise is not apparent in the data presented in Table 3-2.

3.1.2 PHASE NOISE DENSITY

The ionospheric phase noise density referred to 100 MHz, as tabulated in Table 3-4, was derived by transforming the scale of the phase power spectra given in Appendix A. The conversion factor for the scale adjustment for Quinn's data (Figures A-1 through A-8) and Fremouw's et al., data (Figure A-9) was -2.78, -11.56, -13.01 and -21.86 dB, corresponding to the transmission frequency of 137.67, 378.61, 447.44 and 1239.07 MHz, respectively. In the case of Gjeldum's data (Figures A-10 through A-15), the conversion factor was 7.96 and -2.92 dB for the frequencies, 40 and 140 MHz, respectively.

The flatness of Quinn's spectral curves, (i.e., Figures A-1 through A-8) at frequencies less than approximately 0.2 Hz accounts for the constant value of 17.22 dB at 0.02 and 0.2 Hz in Table 3-3.

It is noted that the magnitude of the last data point in the power spectra is assumed to remain constant out to a frequency of 200 kHz. This assumption is evident in the estimates of the phase noise density data shown in Table 3-3.

3.2 DOPPLER EFFECTS

3.2.1 ORBITAL TRAJECTORIES

For this analysis, the propagation effects on the Doppler shift of satellite transmissions were determined on the assumption that the receiving system was located at Boston, Massachusetts (42.5°N, 289°E).

TABLE 3-2

INTEGRATED IONOSPHERIC PHASE NOISE

Observation Site	Pass No.	Transmission Frequency (MHz)	Integrated Phase Noise Frequency Band (Hz – MHz)	Integrated Phase Noise–Standard Deviation (Deg)			Reference
				Transmission Frequency	Extrapolated to 10 GHz	Referred to 100 MHz	
Ancon, Peru	A3R5	137.67	1 – 20 10 – 5	19247.283 9623.453	264.987 132.491	2.650 1.325	Quinn (1980)
	A4R13	137.67	1 – 20 10 – 5	9303.952 4651.674	128.092 64.042	1.281 0.640	
		378.61	1 – 20 10 – 5	7222.199 3610.848	273.437 136.709	2.734 1.367	
		1239.07	1 – 20 10 – 5	4556.650 2278.282	564.602 282.296	5.646 2.823	
	A4R16	137.67	1 – 20 10 – 5	17524.688 8762.116	241.271 120.632	2.413 1.206	
Kwajalein, Marshall Islands	K2R4	137.67	1 – 20 10 – 5	9303.684 4561.678	128.088 64.042	1.281 0.640	
	K4	137.67	1 – 20 10 – 5	9520.466 4760.014	131.073 65.533	1.311 0.655	
		378.61	1 – 20 10 – 5	5554.372 2776.986	210.292 105.138	2.103 1.051	
Poker Flat, Alaska	P3	137.67	1 – 20 10 – 5	4556.817 2278.304	62.736 31.367	0.627 0.314	
	P3R16	137.67	1 – 20 10 – 5	12842.446 6421.093	176.808 88.402	1.768 0.884	
		447.44	1 – 20 10 – 5	811.873 405.158	36.327 18.129	0.363 0.181	
		1239.07	1 – 20 10 – 5	7221.929 3610.838	894.850 447.409	8.949 4.474	
Stanford, California	S1R5	137.67	1 – 20 10 – 5	8987.655 4493.755	123.737 61.867	1.237 0.619	

TABLE 3-2

INTEGRATED IONOSPHERIC PHASE NOISE (CONT)

Observation Site	Pass No.	Transmission Frequency (MHz)	Integrated Phase Noise Frequency Band (Hz – MHz)	Integrated Phase Noise–Standard Deviation (Deg)			Reference
				Transmission Frequency	Extrapolated to 10 GHz	Referred to 100 MHz	
Poker Flat, Alaska	---	137.67	1 – 20 / 10 – 5	541.570 / 270.776	7.456 / 3.728	0.075 / 0.037	Fremouw et al. (1978)
Boulder, Colorado	Set IA	40	1 – 20 / 10 – 5	6436.320 / 3218.157	25.745 / 12.873	0.258 / 0.129	Gjeldum (1978)
		140	1 – 20 / 10 – 5	21809.102 / 10904.539	305.327 / 152.664	3.053 / 1.527	
	Set IB	40	1 – 20 / 10 – 5	9968.678 / 4984.334	39.875 / 19.937	0.398 / 0.199	
		140	1 – 20 / 10 – 5	19214.879 / 9607.430	269.008 / 134.504	2.690 / 1.345	
	Set IIA	40	1 – 20 / 10 – 5	38782.664 / 19391.313	155.131 / 77.565	1.551 / 0.776	
		40	1 – 20 / 10 – 5	17125.283 / 8562.633	68.501 / 34.251	0.685 / 0.343	
	Set IIB	40	1 – 20 / 10 – 5	22836.928 / 11418.452	91.348 / 45.674	0.914 / 0.457	
		140	1 – 20 / 10 – 5	18140.018 / 9069.999	253.960 / 126.980	2.540 / 1.270	
	Set III	40	1 – 20 / 10 – 5	48625.598 / 24132.773	193.062 / 96.531	1.931 / 0.965	
		140	1 – 20 / 10 – 5	8102.847 / 4051.419	113.440 / 56.720	1.134 / 0.567	
	Set IV	40	1 – 20 / 10 – 5	35779.777 / 17889.871	143.119 / 71.560	1.431 / 0.716	
		140	1 – 20 / 10 – 5	109304.406 / 54652.148	1530.262 / 765.130	15.303 / 7.651	

TABLE 3-3

IONOSPHERIC PHASE NOISE DENSITY

Observation Site	Pass No.	Transmission Frequency (MHz)	Phase Noise Density – Referred to 100 MHz (dBc)					Reference
			0.02 Hz	0.2 Hz	2.0 Hz	200 Hz	200 kHz	
Ancon, Peru	A3R5	137.67	—	—	-1.39	-25.27	-25.27	Quinn (1980)
	A4R13	137.67	17.22	17.22	-3.05	-31.58	-31.58	
		378.61	8.44	8.44	-13.67	-42.56	-42.56	
		1239.07	-1.86	-1.86	-29.74	-56.86	-56.86	
	A4R16	137.67	17.22	17.22	-1.10	-26.08	-26.08	
Kwajalein, Marshall Islands	K2R4	137.67	17.22	17.22	-5.26	-31.58	-31.58	
	K4	137.67	17.22	17.22	-4.31	-31.38	-31.38	
		378.61	8.44	8.44	-16.61	-44.84	-44.84	
Poker Flat, Alaska	P3	137.67	17.22	17.22	-8.48	-37.78	-37.78	
	P3R15	137.67	17.22	17.22	-4.80	-28.78	-28.78	
		447.44	6.99	6.99	-20.07	-63.01	-63.01	
		1239.07	-1.86	-1.86	-27.06	-52.86	-52.86	
Stanford, California	S1R5	137.67	17.22	17.22	-8.48	-31.88	-31.88	
Poker Flat, Alaska	--	137.67	-4.28	-4.28	-30.13	-56.28	-56.28	Fremouw et al. (1978)
Boulder, Colorado	Set IA	40	5.5	-20.0	-24.0	-24.0	-24.0	Gjeldum (1978)
		140	-5.4	-21.8	-24.3	-24.3	-24.3	
	Set IB	40	3.0	-17.0	-20.2	-20.2	-20.2	
		140	-5.4	-22.4	-25.4	-25.4	-25.4	
	Set IIA	40	13.0	-7.0	-8.4	-8.4	-8.4	
		40	4.5	-15.5	-15.5	-15.5	-15.5	
	Set IIB	40	6.5	-12.0	-13.0	-13.0	-13.0	
		140	-4.4	-17.4	25.9	-25.9	-25.9	
	Set III	40	8.0	-4.5	-6.5	-6.5	-6.5	
		140	-4.4	-30.4	-32.9	-32.9	-32.9	
	Set IV	40	13.0	-9.0	-9.1	-9.1	-9.1	
		140	1.1	-12.9	-12.9	-12.9	-12.9	

It was assumed that a satellite was traversing (1) a circular polar orbit at an altitude of 500 km and 1000 km and (2) an elliptical polar orbit with an eccentricity of 0.379, an apogee of 10,000 km and a perigee of 1000 km. The projection on the earth's surface of the perigee point coincided approximately with the geographic latitude of Boston.

In addition, a satellite was assumed to be in a geosynchronous orbit (at 35,870-km altitude) with an 8° inclination and stationed at 265.5°E longitude, midway between Boston and Los Angeles (34°N, 242°E).

The ground tracks of a satellite in a geosynchronous orbit and in a circular polar orbit at an altitude of 1000 km are shown in Figure 3-2. The five passes of the elliptical polar orbit evaluated in this report were approximately identical to the circular orbit illustrated in Figure 3-2. For the 500-km altitude circular polar orbit, the equatorial crossing of the satellite, i.e., longitude of the ascending node (LAN), occurred at 269°E, 279°E, 289°E, 299°E and 309°E. The longitude of the ascending node of 289°E corresponds to the longitude of Boston.

The elevation angle as observed from Boston for a satellite in a circular polar orbit at an altitude of 1000 km is shown in Figure 3-3. Although the satellite crossed the equator at the same longitude of Boston, the maximum elevation angle is on the order of only 73°, mainly because of the earth's rotation.

Figure 3-4 is a plot of the elevation angle, as observed from Boston and Los Angeles, for a satellite at geosynchronous altitude. For Boston, the elevation angle of the satellite varies between approximately 28° and 43° while for Los Angeles, the angle varies between 36° and 51°. The difference in the elevation angles is attributed to the difference in the latitudes of two locations.

The Doppler frequency shift at a frequency of 100 MHz as observed from Boston for a satellite in a 1000-km altitude circular polar orbit and in an elliptical polar orbit are presented in Figures 3-5 and 3-6, respectively. The Doppler shift is a maximum for a satellite with a LAN of 289°E and a minimum with a LAN of 259°E. When neglecting the effects of the propagation media, the maximum Doppler shift is on the order of 2118 Hz for the circular orbit, as compared to about 2520 Hz for the elliptical orbit.
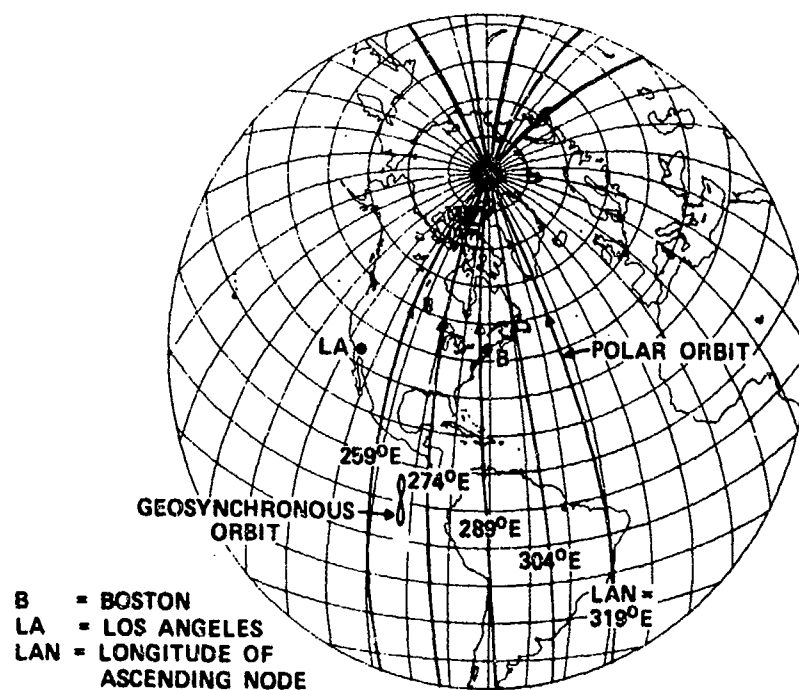
Figure 3-2. Ground Tracks of a Satellite at Geosynchronous Altitude
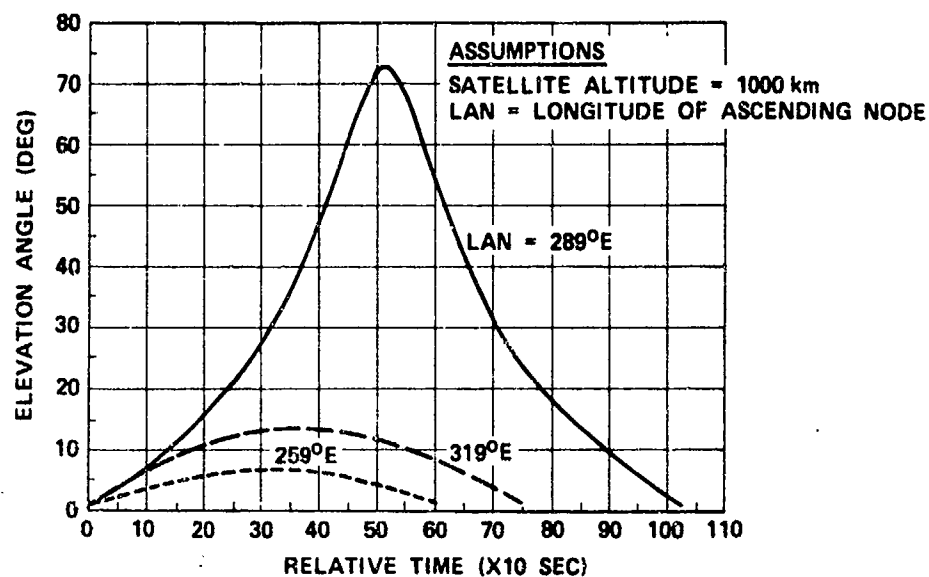and in a Circular Polar Orbit at an Altitude of 1000 km

Figure 3-3. Elevation Angle as Observed from Boston for a
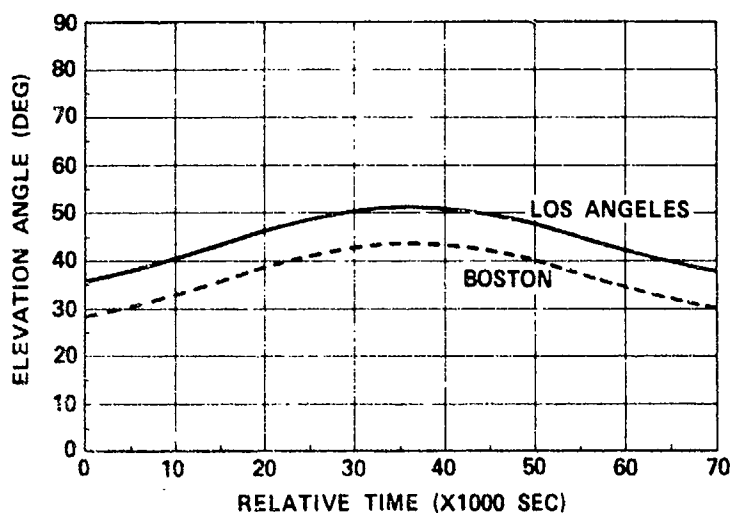Satellite in a Circular Polar Orbit

Figure 3-4. Elevation Angle as Observed from Boston and
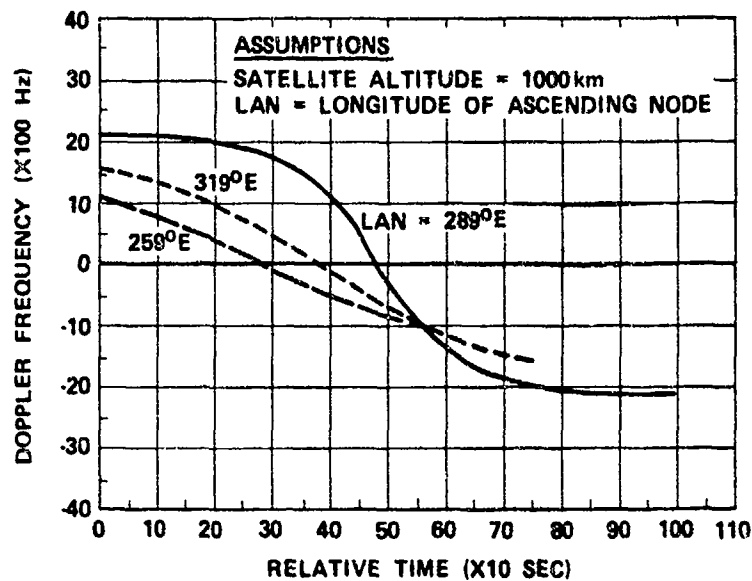Los Angeles for a Satellite at Geosynchronous
Altitude

Figure 3-5. Doppler Frequency Shift at 100 MHz as Observed from Boston for a Satellite in a Circular Polar Orbit
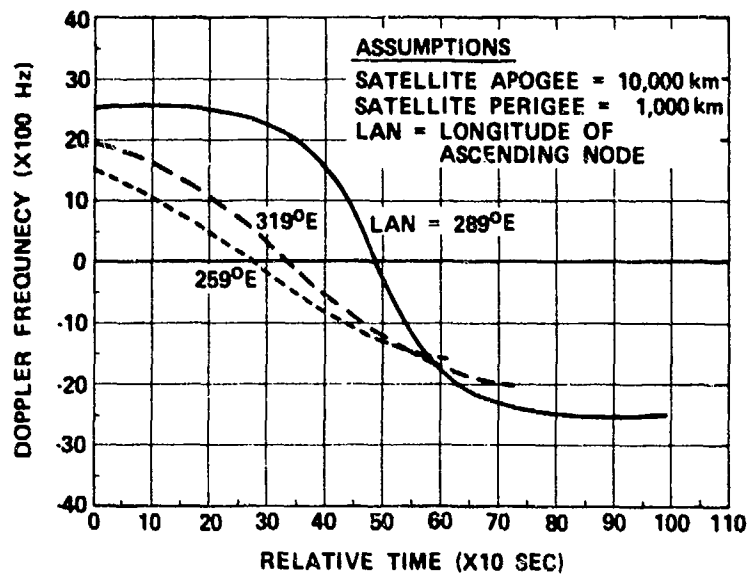

Figure 3-6. Doppler Frequency Shift at 100 MHz as Observed from Boston for a Satellite in an Elliptical Polar Orbit

It is seen that the Doppler shift is positive for a satellite approaching Boston and negative as it recedes from Boston. Zero Doppler occurs at the point of closest approach. For a satellite in a circular polar orbit at 500-km altitude, the maximum Doppler shift at 100-MHz frequency evaluates to 2354 Hz as compared to 2118 Hz for a satellite at an altitude of 1000 km. It is noted that, at 100 MHz, the maximum Doppler frequency shift of transmissions from the satellite in the geosynchronous orbit is about 17 Hz.

According to Equation (2-18), the Doppler frequency shift is directly proportional to the transmission frequency and the satellite velocity. The velocity of a satellite, V, in an elliptical orbit is given by

$$V = \left[m g \left(\frac{2}{r} - \frac{1}{a} \right) \right]^{1/2} \tag{3-1}$$

where m is the mass of the earth (5.975×10^{24} kg), g is the gravitational constant (6.67×10^{-11} m^3/sec^2 -kg), r is the radial distance of the satellite from the earth's center and a is the semimajor axis of the ellipse.

For a satellite in a circular orbit, the semimajor axis reduces to the radial distance r. It follows that the velocity of a satellite in a circular orbit at an altitude of 500, 1000 and 2000 km evaluates to 7.616, 7.353 and 6.900 km/sec, respectively.

3.2.2 TROPOSPHERIC EFFECTS

According to Equations (2-33), (2-34) and (2-35), the Doppler frequency error is a function of ΔE, the ground elevation angle error induced by the refraction phenomenon. The parameter, ΔE, for an altitude of 1000 km is presented in Figure 3-7 as a function of surface refractivity and elevation angle. It is evident that the angular bending error increases with increasing surface refractivity and with decreasing elevation angle.

It is noted that the elevation angle error is also a function of altitude. At 1° elevation angle and a surface refractivity of 320 N-units, ΔE evaluates to 8.06, 8.22 and 8.53 mrad at 500 km, 1000 km and geosynchronous altitude, respectively. The effect of altitude on the magnitude of ΔE diminishes as the elevation angle increases. For example, at 15° elevation angle, the value of ΔE at the three altitudes approaches 1.15, 1.16, and 1.17 mrad, respectively.
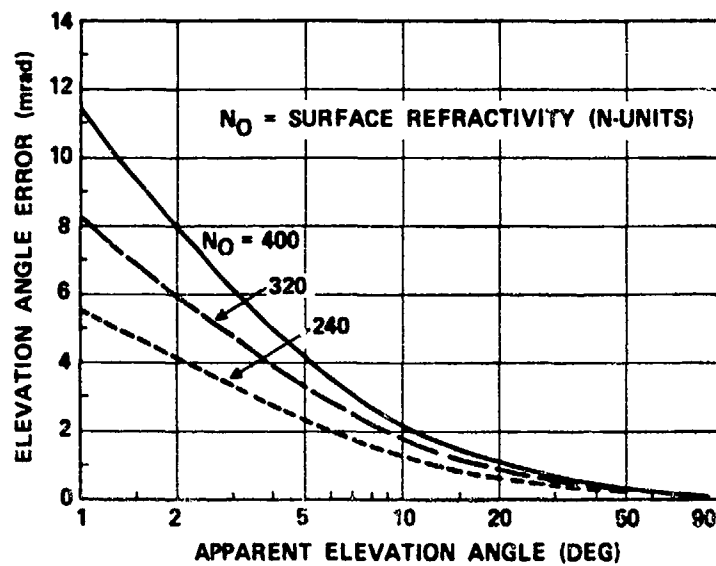
Figure 3-7. Tropospheric Elevation Angle Error at 1000-km
Altitude Based on CRPL Reference Atmosphere - 1958

Figure 3-8 depicts the tropospheric Doppler error at 100 MHz for the 1000-km circular polar orbit. The Doppler error is about 0.50 Hz for a surface refractivity of 320 N-units and increases to about 0.67 Hz for a surface refractivity of 400 N-units. At 10 GHz, the Doppler error would increase to 50 and 67 Hz, respectively.

The interesting feature to note in Figure 3-8 is that the Doppler error is a maximum at the two extremes of the orbital pass. According to Figure 3-3, this corresponds to the lowest elevation angle. An examination of Figures 3-3 and 3-8 also reveals that, as the elevation angle increases, the Doppler error decreases, and that the error is less than 0.1 Hz for elevation angles greater than about 25°.

The effect of satellite altitude on the Doppler error is demonstrated in Figure 3-9. It is clearly evident that, for a given elevation angle, the error varies inversely with altitude. The disclosure that the altitude – Doppler error inverse relationship also applies to the elliptical orbit is unexpected. It was anticipated that the Doppler error would follow in the same manner as the data in Figures 3-5 and 3-6. That is, a satellite in an extreme elliptical orbit imparts a greater Doppler frequency shift than one in an 1000-km altitude circular orbit.

With regard to the geosynchronous orbit, the maximum Doppler error at 100 MHz is approximately 1.2×10^{-4} Hz for a surface refractivity of 320 N-units.

3.2.3 IONOSPHERIC EFFECTS

The ionospheric refraction angle error, used in this analysis, is shown in Figure 3-10. The calculations are based on a frequency of 100 MHz and a vertical electron content of 10^{18} electrons/m^2. An interesting feature of this plot is that, at a constant altitude of 1000 km, the error increases with elevation angle, attaining a maximum value of 8.3 mrad at about 5°. In the case of the troposphere, however, the elevation angle error monotonically decreases with elevation angle as indicated in Figure 3-7.

Figure 3-11 is a plot of the Doppler error at 100 MHz that occurs when ionospheric refraction effects are taken into account. The calculations apply to a satellite in a circular polar orbit at 1000-km altitude. It is of interest to note that the error varies cyclically as the satellite traverses its orbital pass. This is in contrast to Figures 3-8 and 3-9 which depict the Doppler errors induced by the troposphere.
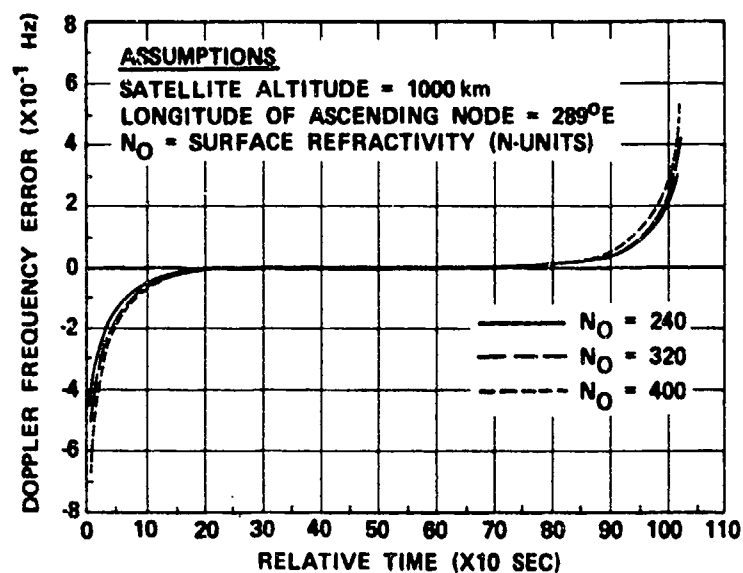
Figure 3-8. Tropospheric Doppler Frequency Error at 100 MHz
as Observed from Boston for a Satellite in a
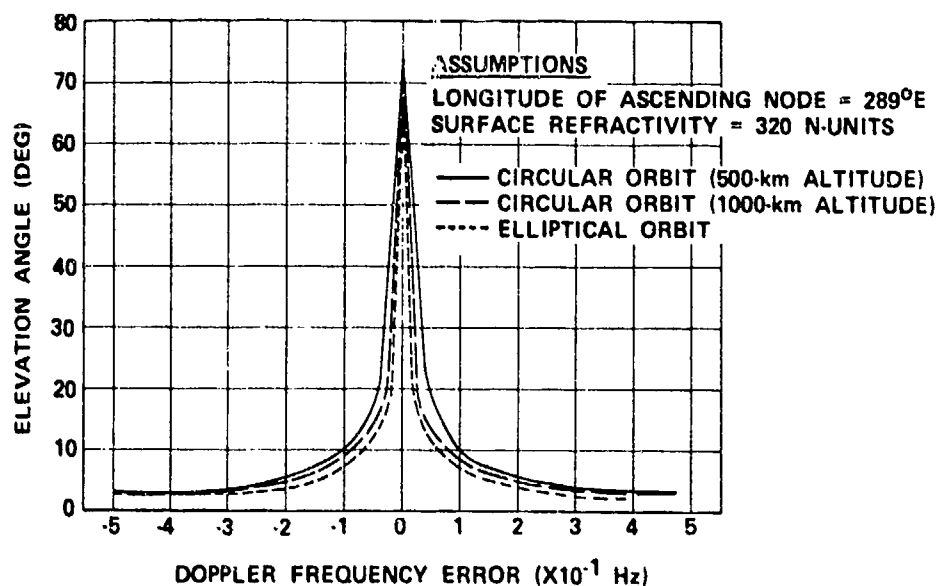Circular Polar Orbit

Figure 3-9. Tropospheric Doppler Frequency Error at 100 MHz as Observed
from Boston for a Satellite in Circular and Elliptical Polar Orbits
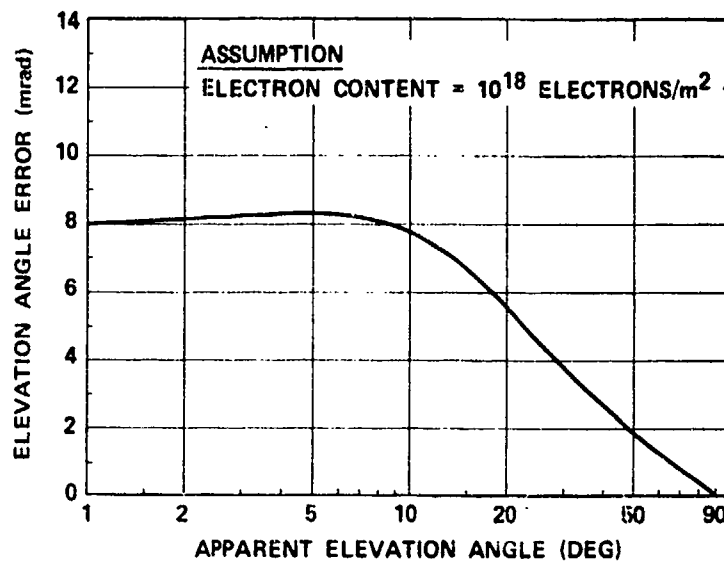
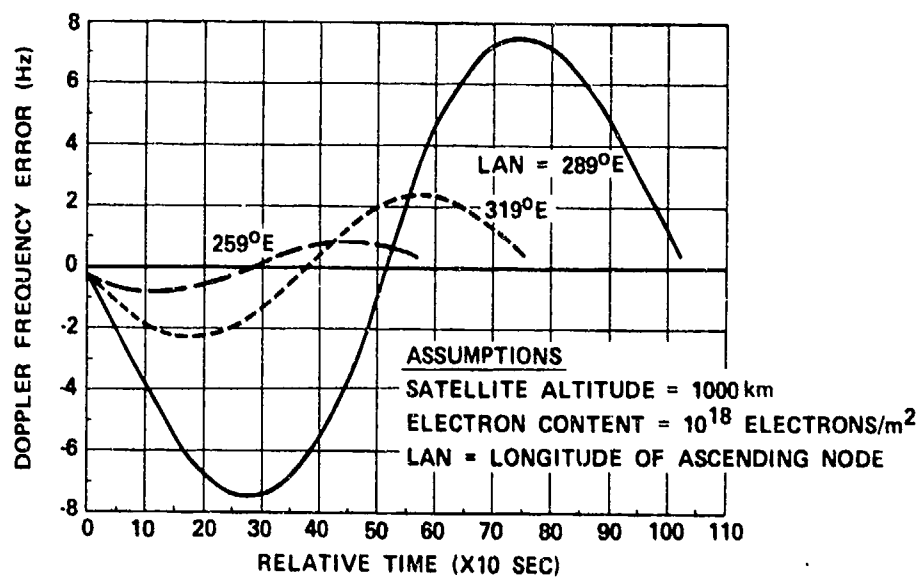Figure 3-10. Ionospheric Elevation Angle Error at 1000-km Altitude, 100 MHz

Figure 3-11. Ionospheric Doppler Frequency Error at 100 MHz as Observed from Boston for a Satellite in a Circular Polar Orbit

As shown in Figure 3-11, for a LAN of 289°E, the Doppler error maximizes at a relative time of approximately 250 and 720 sec which, according to Figure 3-3, correspond to an elevation angle of about 25°. It is evident that the elevation angle at which the maximum Doppler error occurs is dependent on the LAN of the orbital pass. It can be readily deduced that, for an LAN of 259°E and 319°E, the elevation angles of the maximum Doppler error are about 5° and 9°, respectively.

The ionospheric Doppler frequency errors for a satellite in an elliptical polar orbit, illustrated in Figure 3-12, are less than those of a satellite in a circular polar orbit given in Figure 3-11. These results are in agreement with the tropospheric data presented in Figure 3-9.

For the geosynchronous orbit, the maximum Doppler error at 100 MHz is on the order of 2×10^{-2} Hz, the calculations being based on an electron content of 10^{18} electrons/m^2.

The effect of a change in frequency and electron content on the Doppler error is shown in Figure 3-13. It is seen that, when the frequency is decreased to 50 MHz, the Doppler error increases by a value ranging between 1.5 and 2. The variation is a function of the elevation angle, the maximum taking place in the vicinity of the point of closest approach. When the electron content is increased by an order of magnitude, there is an increase in the Doppler error by a factor of 5 to 10. The range of values is also attributed to the elevation angle dependency.

It is noted that, for a satellite in a circular polar orbit at an altitude of 1000 km, the maximum ionospheric Doppler error at 100 MHz is a factor of about 15 larger than that due to the troposphere. At a frequency of 1000 MHz, the ratio of the two contributions reduces to 0.15. The reduction is due to the fact that the tropospheric Doppler error is directly proportional to frequency, and that the ionospheric error is approximately inversely proportional to frequency.

The frequency shift resulting from a change in the vertical electron content along the satellite orbit, as described in Equation (2-51), is not considered in detail in this paper. However, it is estimated that, in the presence of a traveling ionospheric disturbance (TID) which is a large-scale electron-density perturbation in the F-region of the ionosphere, a Doppler shift perturbation of 0.14 Hz could occur at a frequency of 100 MHz (Millman, 1980). The calculations are based on an ambient electron content of 10^{18} electrons/m^2 and on a TID with a horizontal velocity of 200 m/sec, a dimension of 150 km and a modulation of 2% on the ambient electron content.
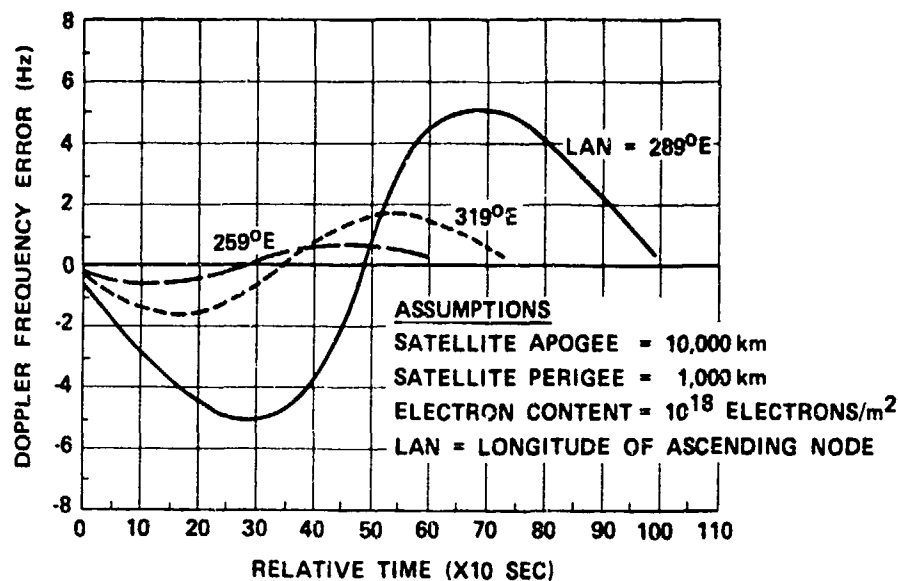
Figure 3-12. Ionospheric Doppler Frequency Error at 100 MHz as Observed from Boston for a Satellite in an Elliptical Polar Orbit
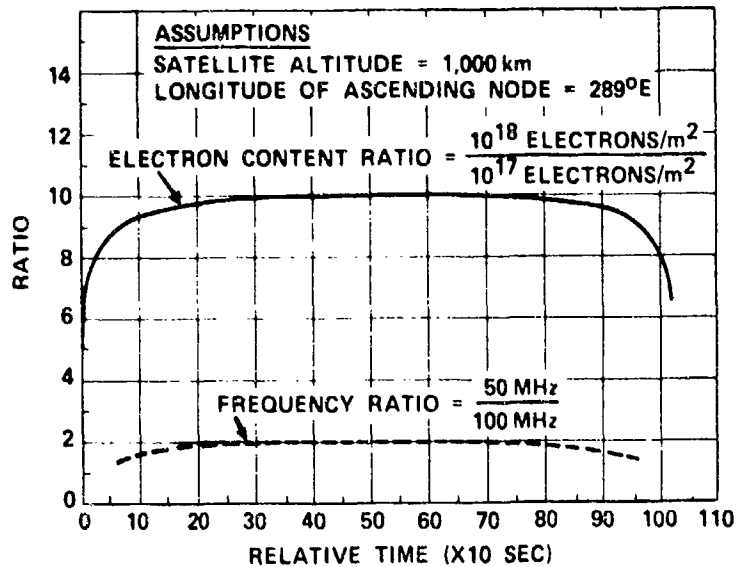

Figure 3-13. Ratio of Ionospheric Doppler Frequency Error as Observed from Boston for a Satellite in a Circular Polar Orbit

SECTION IV

CONCLUSIONS

The rms phase fluctuations introduced by the troposphere are estimated to be on the order of 9° – 90° for a transmission frequency of 10 GHz and an elevation angle of 5°. The spread in the estimation is basically due to the uncertainty of the characteristics of the tropospheric turbulence. The rms phase fluctuations will decrease as the elevation angle is increased.

For a transionospheric propagation path, the tropospheric phase fluctuations can be eliminated by transmitting two coherent, harmonically related signals.

With regard to the ionosphere, the rms phase fluctuations at 10 GHz are theoretically predicted to be at least an order of magnitude less than the tropospheric values.

Extrapolation of ground-based measurements of satellite ultra-high frequency (UHF) radio wave transmissions reveals that, at 10 GHz, the standard deviation of the phase fluctuations in the ionosphere could be between 0.09° and 3.14°. At 1 GHz, the spread in the standard deviation of the phase fluctuations could range between 1.21° and 49.85°. The wide variations may be due to the geographic location of the observation sites.

The statistical characteristics of the standard deviation of the integrated ionospheric phase noise at 10 GHz (referred to 100 MHz), summarized in Table 4-1, show that the median value in a frequency band of 1 Hz – 20 MHz could be on the order of 1.491°. By reducing the upper frequency limit to 5 MHz, the integrated phase noise decreases by a factor of one-half.

A summary of the ionospheric phase noise density statistics at 10 GHz (referred to 100 MHz), given in Table 4-2, reveals that, at 2×10^{-2} Hz, the median value could be as high as 7.0 dBc and decrease to -26.1 dBc at 2×10^{5} Hz.

TABLE 4-1

INTEGRATED IONOSPHERIC PHASE NOISE AT 10 GHz REFERRED TO 100 MHz

Frequency Band	Integrated Phase Noise - Standard Deviation (Deg)			
	Minimum	Mean	Maximum	Median
1 Hz - 20 MHz	0.075	2.474	15.303	1.491
10 Hz - 5 MHz	0.037	1.237	7.651	0.746

TABLE 4-2

IONOSPHERIC PHASE NOISE DENSITY AT 10 GHz REFERRED TO 100 MHz

Frequency (Hz)	Phase Noise Density (dBc)		
	Minimum	Maximum	Median
2×10^{-2}	−5.4	17.2	7.0
2×10^{-1}	−17.4	17.2	−4.3
2×10^{0}	−32.9	−1.4	−13.0
2×10^{2}	−63.0	−6.1	−26.1
2×10^{5}	−63.0	−6.1	−26.1

The refraction phenomenon in the troposphere and the ionosphere introduces an error in the Doppler frequency shift of satellite transmissions. The Doppler error imposed by the troposphere is directly proportional to frequency while, in the case of the ionosphere, the error is approximately inversely proportional to the frequency and approximately directly proportional to the vertical electron content.

Under average tropospheric and ionospheric conditions, i.e., surface refractivity equal to 320 N-units and electron content equal to 10^{18} electrons/m^2, the tropospheric contribution to the Doppler error is predominant for frequencies on the order of 400 MHz and above. Below about 400 MHz, the ionospheric refraction effects are prevalent.

The Doppler effects can be compensated for, to some extent, when the angular bending and the space vehicle velocity are known. Estimates of the angular bending due to the troposphere can be made to a fair degree of accuracy, from measurements of the surface refractivity. For the ionosphere, the vertical electron content data can be used for the estimation of the refraction angle error.

SECTION V

REFERENCES

Aarons, J., "Global Morphology of Ionospheric Scintillations", Proceedings of the IEEE, Vol. 70, pp. 360-378, April 1982.

Bean, B.R., and E.J. Dutton, "Radio Meteorology", National Bureau of Standards Monograph 92, March 1966.

Bean, B.R., and C.B. Emmanuel, "Spectral Interdependence of the Radio Refractivity and Water Vapor in the Atmosphere", Radio Science, Vol. 4, pp. 1159-1162, December 1969.

Booker, H.G., "The Use of Radio Stars to Study Irregular Refraction of Radio Waves in the Ionosphere", Proceedings IRE, Vol. 46, pp. 298-314, 1958.

CCIR, "Ionospheric Effects Upon Earth - Space Propagation", Report 263-4, XVth Plenary Assembly, Geneva, 1982.

Crane, R.K., "Ionospheric Scintillation", Proceedings IEEE, Vol. 65, pp. 180-199, February 1977.

Crane, R.K., "Morphology of Ionospheric Scintillation", Lincoln Laboratory, Technical Note 1974-29, May 1974.

Crane, R.K., "Ray-Tracings in Cloud Cross Sections for a Long Baseline Interferometer", Proceedings of the 3rd Tropospheric Refraction Effects Meeting, Technical Documentary Report No. ESD-TDR-64-148, The Mitre Corporation, Vol. 1, pp. 57-74, November 1964.

Davies, K., "Ionospheric Radio Propagation", National Bureau of Standards Monograph 80, April 1965.

Deam, A.P., and B.M. Fannin, "Phase-Difference Variations in 9350-Megacycle Radio Signals Arriving at Space Antennas", Proceedings IRE, Vol. 43, pp. 1402-11, October 1955.

Fremouw, E.J., R.L. Leadabrand, R.C. Livingston, M.D. Cousins, C.L. Rino, B.C. Fair and R.A. Long, "Early Results from the DNA Wideband Satellite Experiment - Complex-Signal Scintillation", Radio Science, Vol. 13, pp. 167-187, 1978.

Gjeldum, R.J., "Multifrequency Studies of Ionospheric Phase Scintillation", in "Experimental and Theoretical Studies of Transionospheric Radio Signals", University of Illionois, Technical Report No. 63, UILU-ENG-78-2541, pp. 1-52, April 1978.

Herbstreit, J.W., and M.C. Thompson, "Measurements of the Phase of Radio Waves Received over Transmission Paths with Electrical Lengths Varying as a Result of Atmospheric Turbulence", Proceedings IRE, Vol. 43, pp. 1391-1401, October 1955.

Lane, J.A., "Scintillation and Absorption Fading on Line-of-Sight Links at 35 and 100 GHz", paper presented at the Conference on Tropospheric Wave Propagation, London, England, September - October 1968.

Meyer, J.H., "Digital Atmospheric Profile Generation", Proceedings of the 3rd Tropospheric Refraction Effects Meeting, Technical Documentary Report No. ESD-TDR-64-148, the Mitre Corporation, Vol. 1, pp. 43-56, November 1964.

Millman, G.H., "Atmospheric Effects on VHF and UHF Propagation", Proceedings IRE, Vol. 46, pp. 1492-1501, August 1958.

Millman, G.H., "A Survey of Tropospheric, Ionospheric and Extraterrestrial Effects on Radio Propagation Between the Earth and Space Vehicles", General Electric Technical Information Series Report No. R66EMH1, January 1966 (also published in Propagation Factors in Space Communications, AGARD Conference Proceedings No. 3, pp. 3-55 Technivision, 1967).

Millman, G.H., "An Analysis of Ionospheric Phase Fluctuations Following a Magnetic Disturbance", General Electric Technical Information Series Report No. R78EMH6, October 1978.

Millman, G.H., "Ionospheric Electron Content Effects on Earth-Space Radio Propagation - A Review", General Electric Technical Information Series Report No. R80EMH11, December 1980.

Millman, G.H., and R.E. Anderson, "TRANSIT Satellite Observations of Ionospheric Irregularities", in Propagation Limitations of Navigational and Positioning Systems, AGARD Conference Proceedings No. 209, pp. (4-1) - (4-14), February 1977.

Millman, G.H., and G.M. Reinsmith, "An Analysis of the Incoherent Scatter - Faraday Rotation Technique for Ionospheric Propagation Error Correction", General Electric Technical Information Series Report No. R74EMH2, February 1974.

Muchmore, R.B., and A.D. Wheelon, "Line-of-Sight Propagation Phenomena - I Ray Treatment", Proceedings IRE, Vol. 43, pp. 1437-1449, October 1955.

Quinn, S.B., "Studies of Transionospheric Scintillation Using Orbiting Satellite Data", University of Illinois, Scientific Report No. 2, AFGL-TR-80-0092, April 1980.

Rino, C., J. Petriceks, R. Livingston and C. Dawson, "Data Reduction and Analysis of Coherent Satellite Transmissions", SRI International, Final Report, Contract No. F19628-76-C-0251, December 1977.

Smith, E.K., and S. Weintraub, "The Constants in the Equation for Atmospheric Refractive Index at Radio Frequencies", Proceedings IRE, Vol. 41, pp. 1035-1037, August 1953.

Tatarski, V.I., "Wave Propagation in a Turbulent Medium", (translated by R.A. Silverman), McGraw-Hill Book Co., Inc., New York, 1961.

Weaver, T.S., and D.L. Ringwalt, "Simultaneous Refractive Index Measurements by Three Aircraft", Proceedings of the 3rd Tropospheric Refraction Effects Meeting, Technical Documentary Report No. ESD-TDR-64-148, The Mitre Corporation, Vol. 1, pp. 9-31, November 1964.

Wickerts, S., "Om Finestrukturen Hos Atmosfärens Brytningsindexfält", Research Institute of National Defence (Sweden), FOA 3 Report A660, February 1960.

APPENDIX A

IONOSPHERIC PHASE SCINTILLATION SPECTRAL DATA

The ionospheric phase scintillation spectral data used in the evaluation of the integrated phase noise and the phase noise density described in par. 3.1, are presented in Figures A-1 through A-15.

The frequencies designated by Quinn (1980) in Figures A-1 through A-8 and by Fremouw et al., (1976) in Figure A-9 in terms of the notation, VHF, UHF1, UHF2 and L-band refer to 137.6748, 378.6057, 447.4431 and 1239.073 MHz, respectively.

The symbol NN in Figures A-10 through A-15 is the inverse of the filter cut-off frequency. It indicates the frequencies below 1/NN which were discarded by Gjeldum (1978) in his analysis of the phase scintillation data.
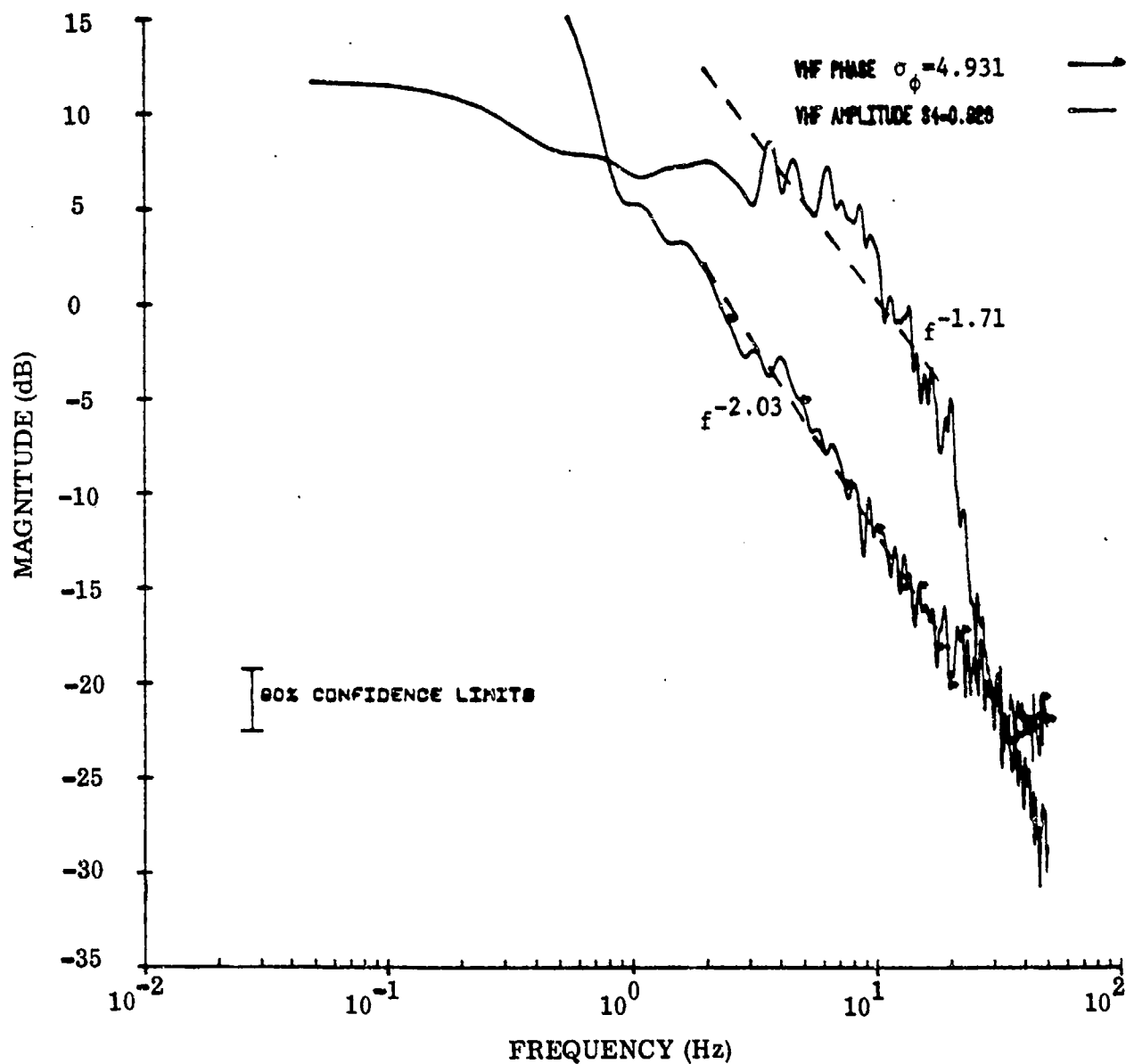
Figure A-1. Pass A3R5 Power Spectra (After Quinn, 1980)
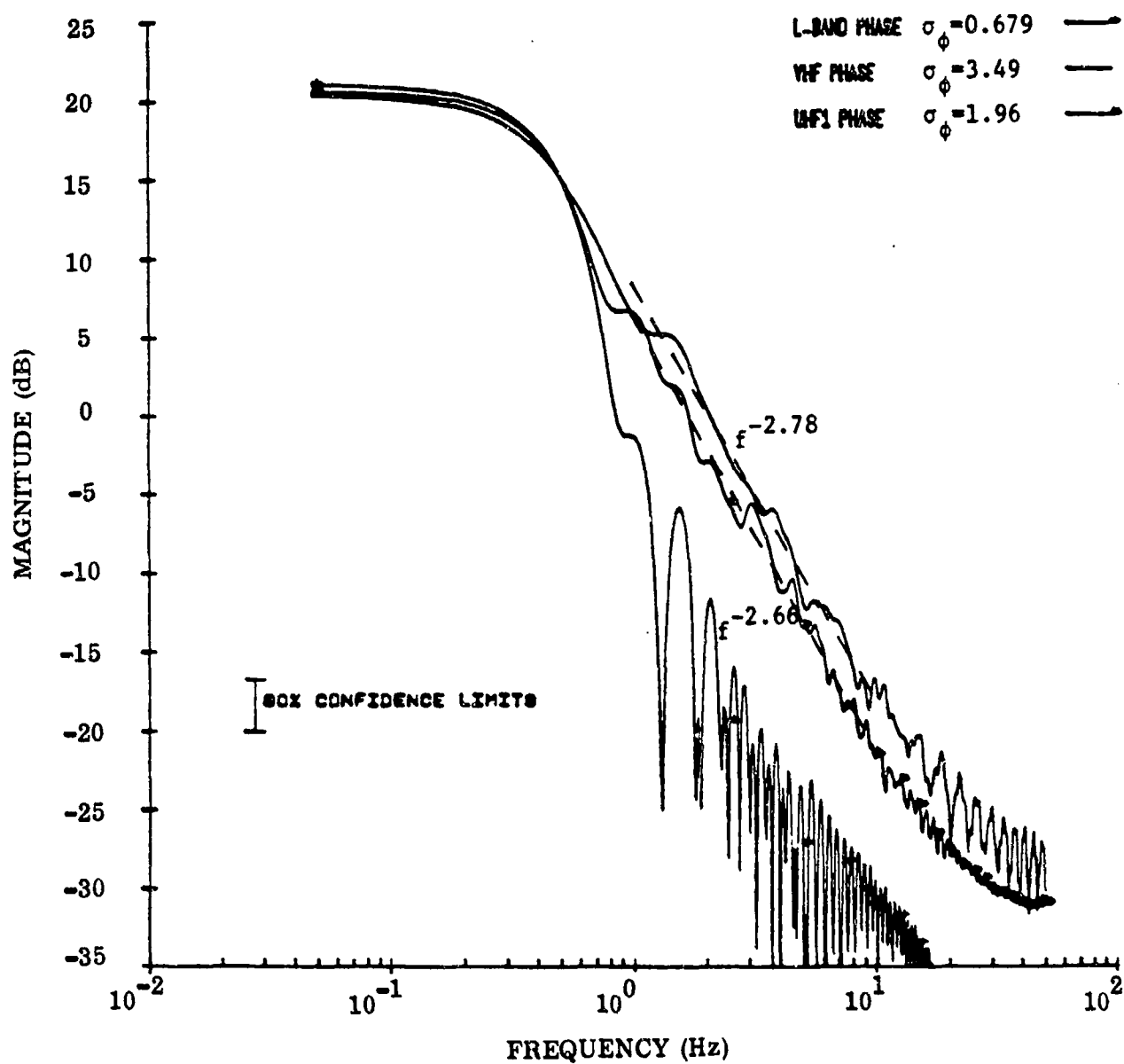
Figure A-2. Pass A4R13 Power Spectra (After Quinn, 1980)

A-3
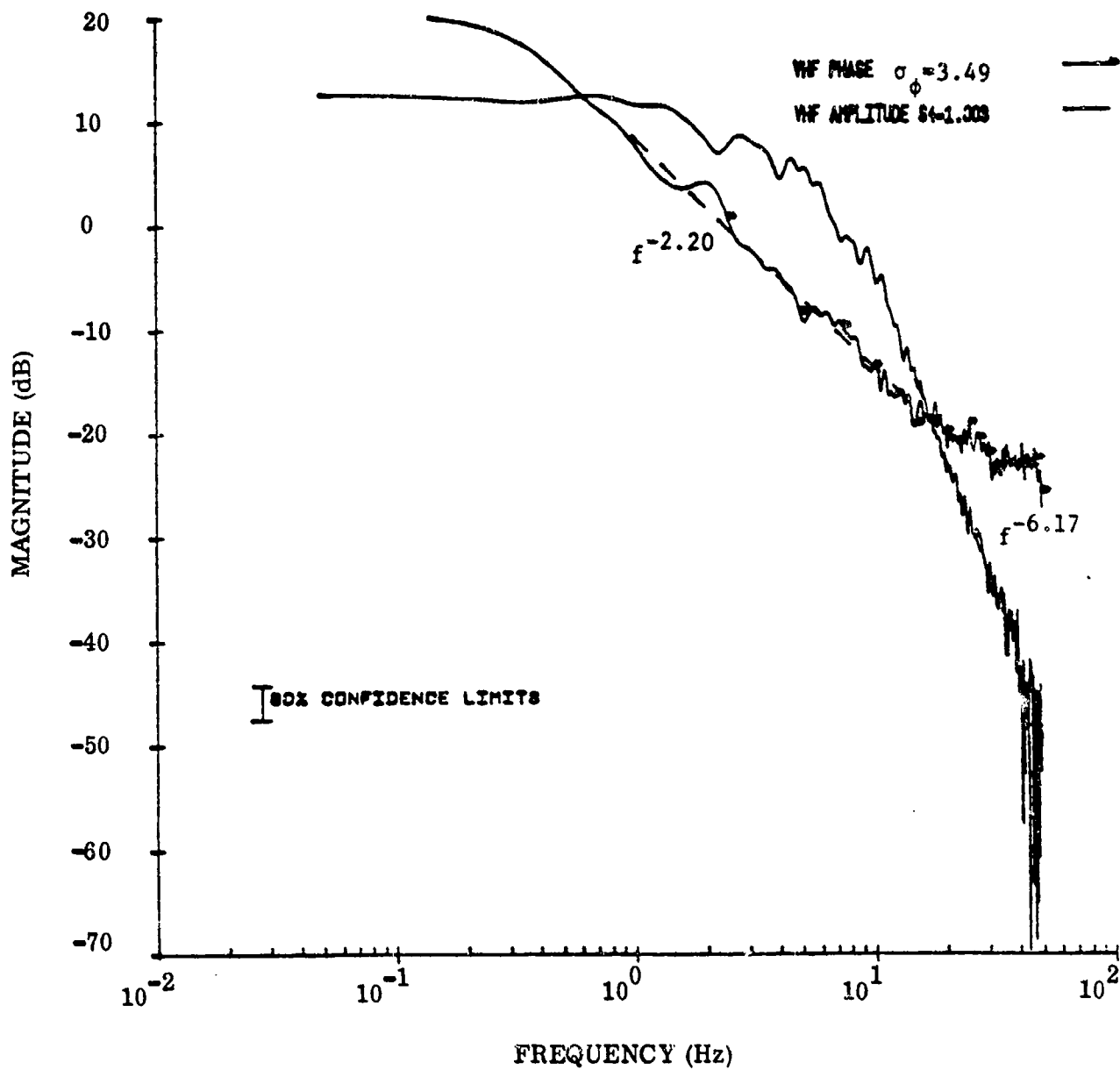
Figure A-3. Pass A4R16 Power Spectra (After Quinn, 1980)
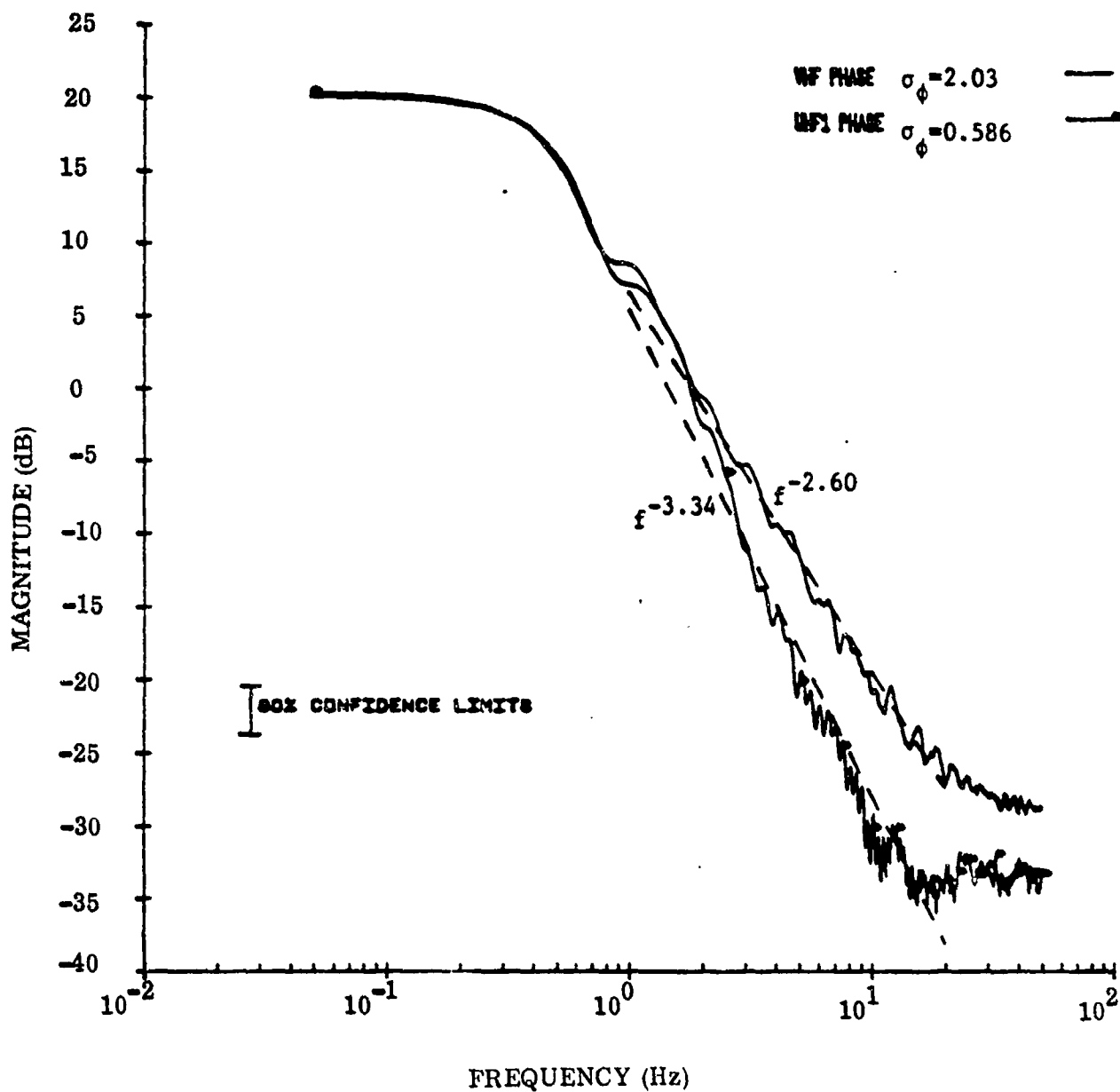
Figure A-4. Pass K4 Phase Spectra (After Quinn, 1980)
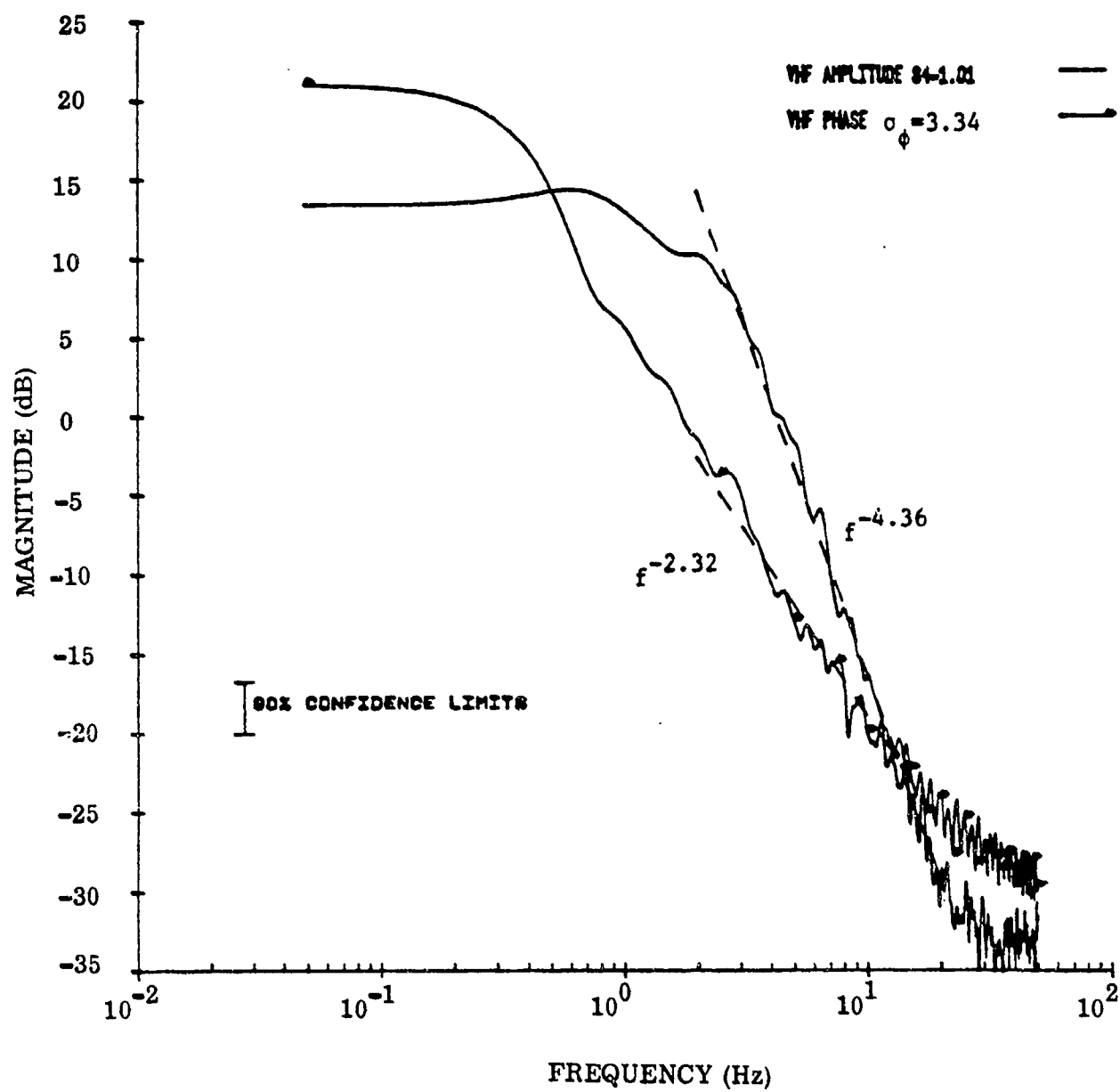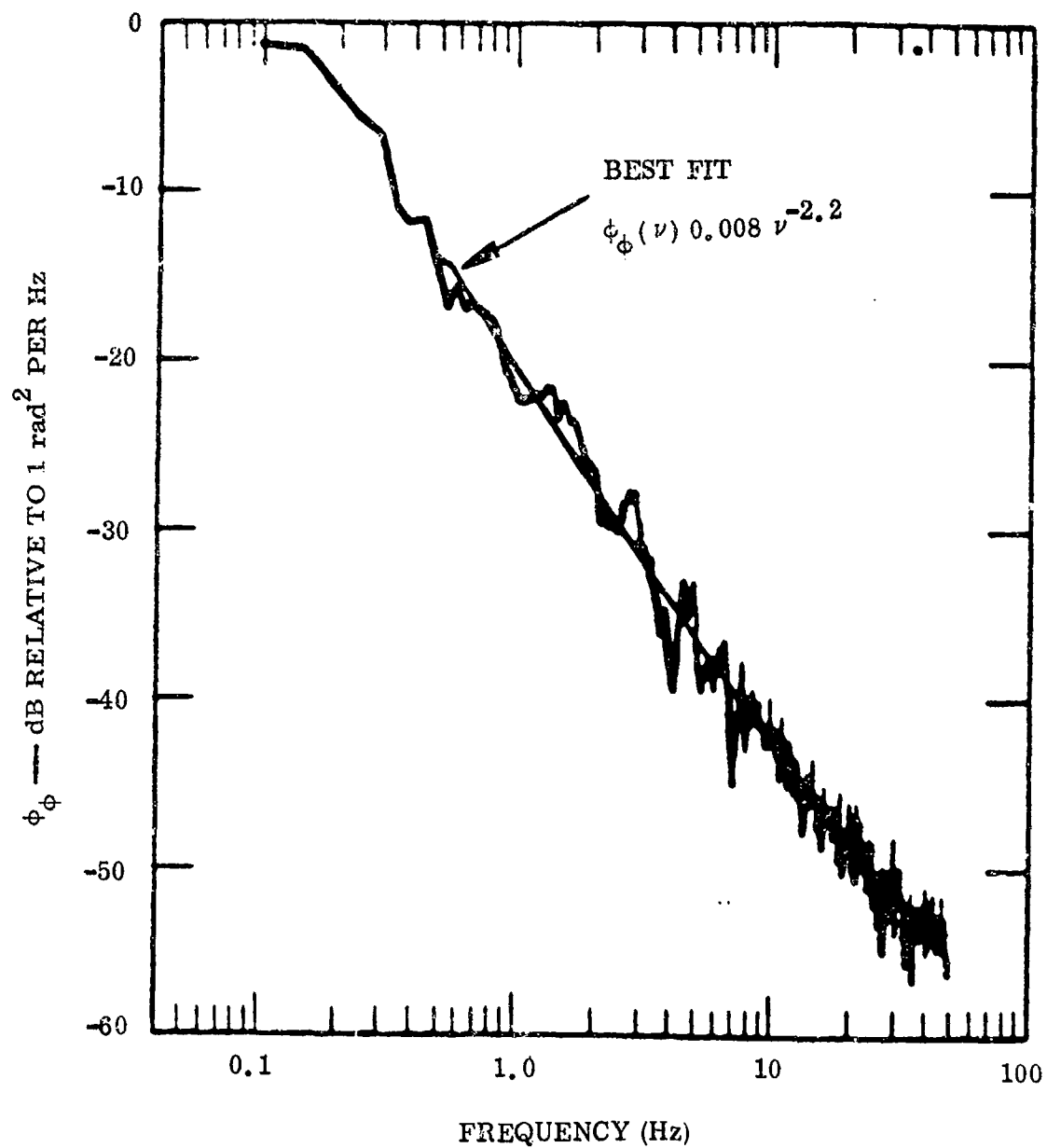
Figure A-5. Pass K2R4 Power Spectra (After Quinn, 1980)

A-6
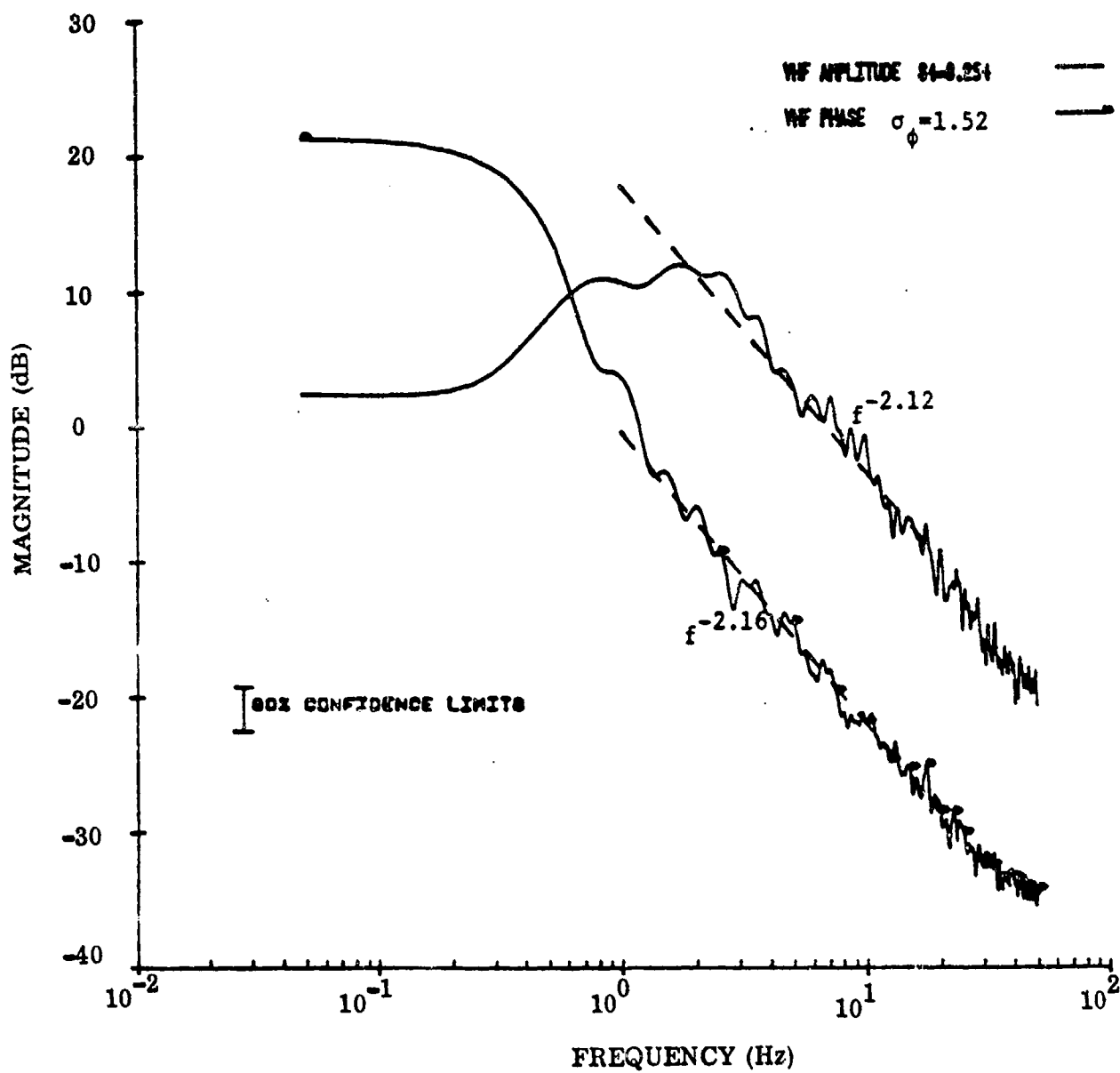
Figure A-6. Pass P3 Power Spectra (After Quinn, 1980)
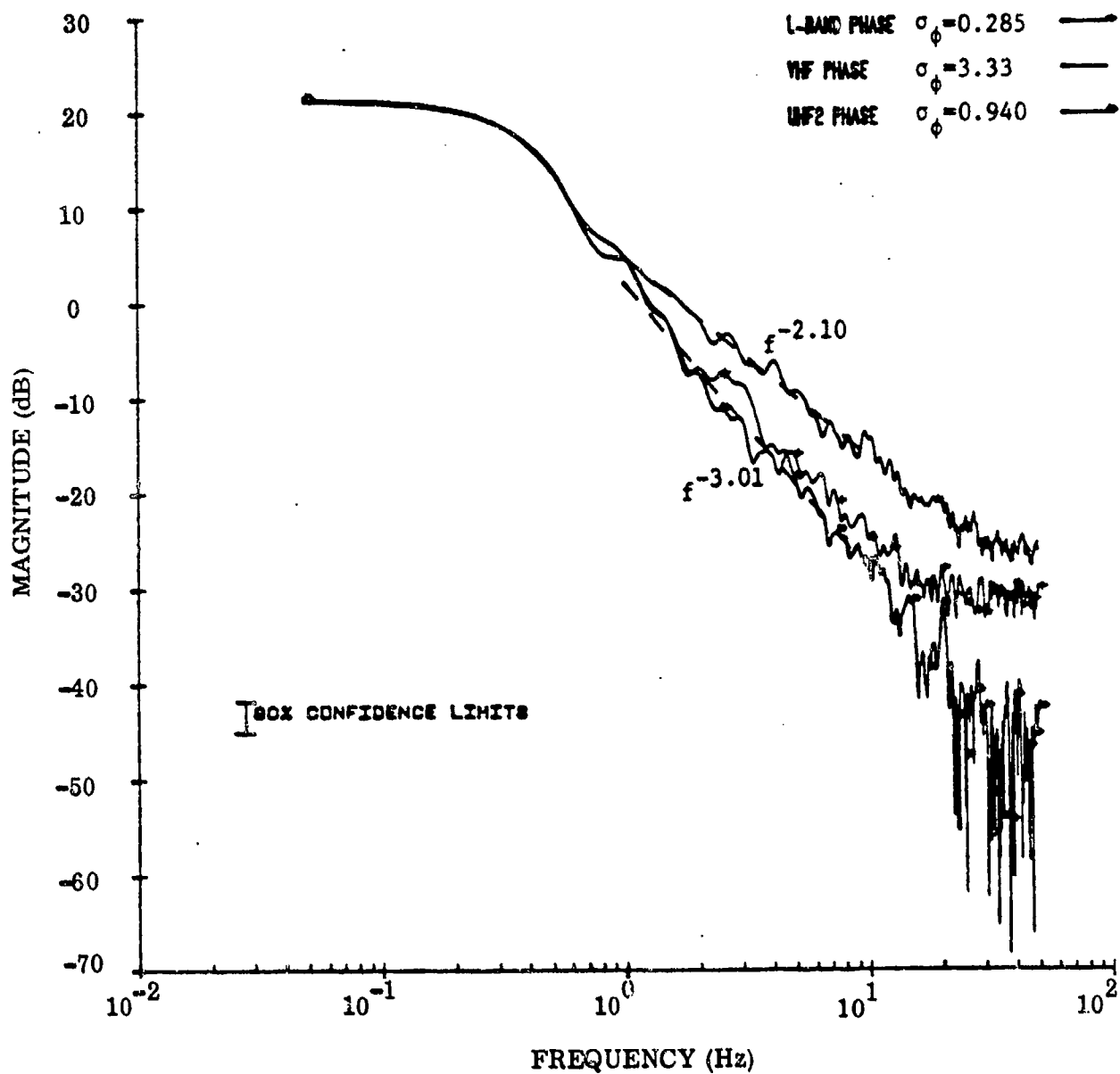
Figure A-7. Pass P3R16 Phase Spectra (After Quinn, 1980)
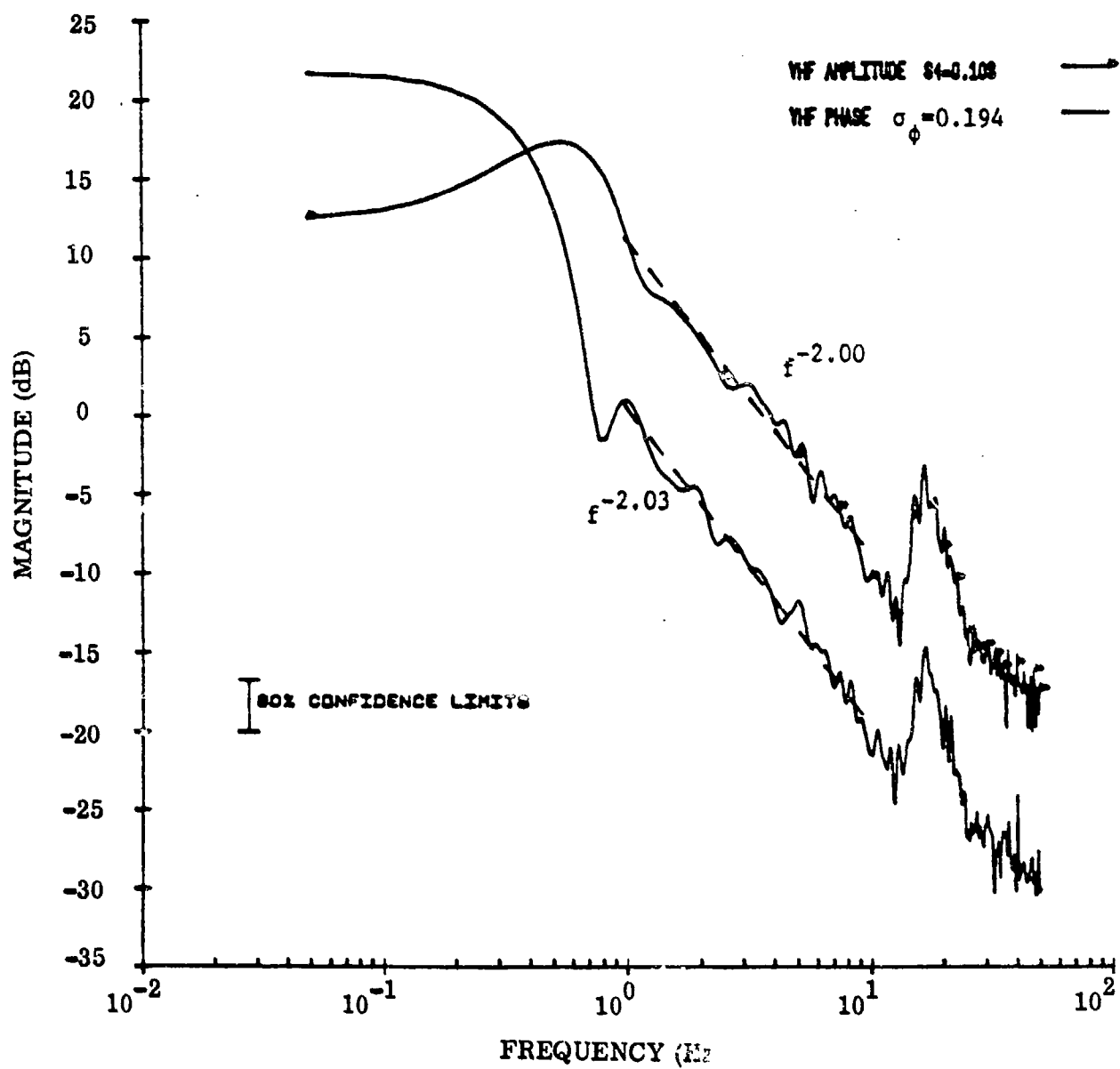
Figure A-8. Pass S1R5 Power Spectra (After Quinn, 1980)

A-9

Figure A-9. Power Spectrum of VHF Phase for a 10-sec Portion of Poker Flat Pass 7-35, 27 August 1976, 1244 UT. (After Fremouw et. al., 1978)
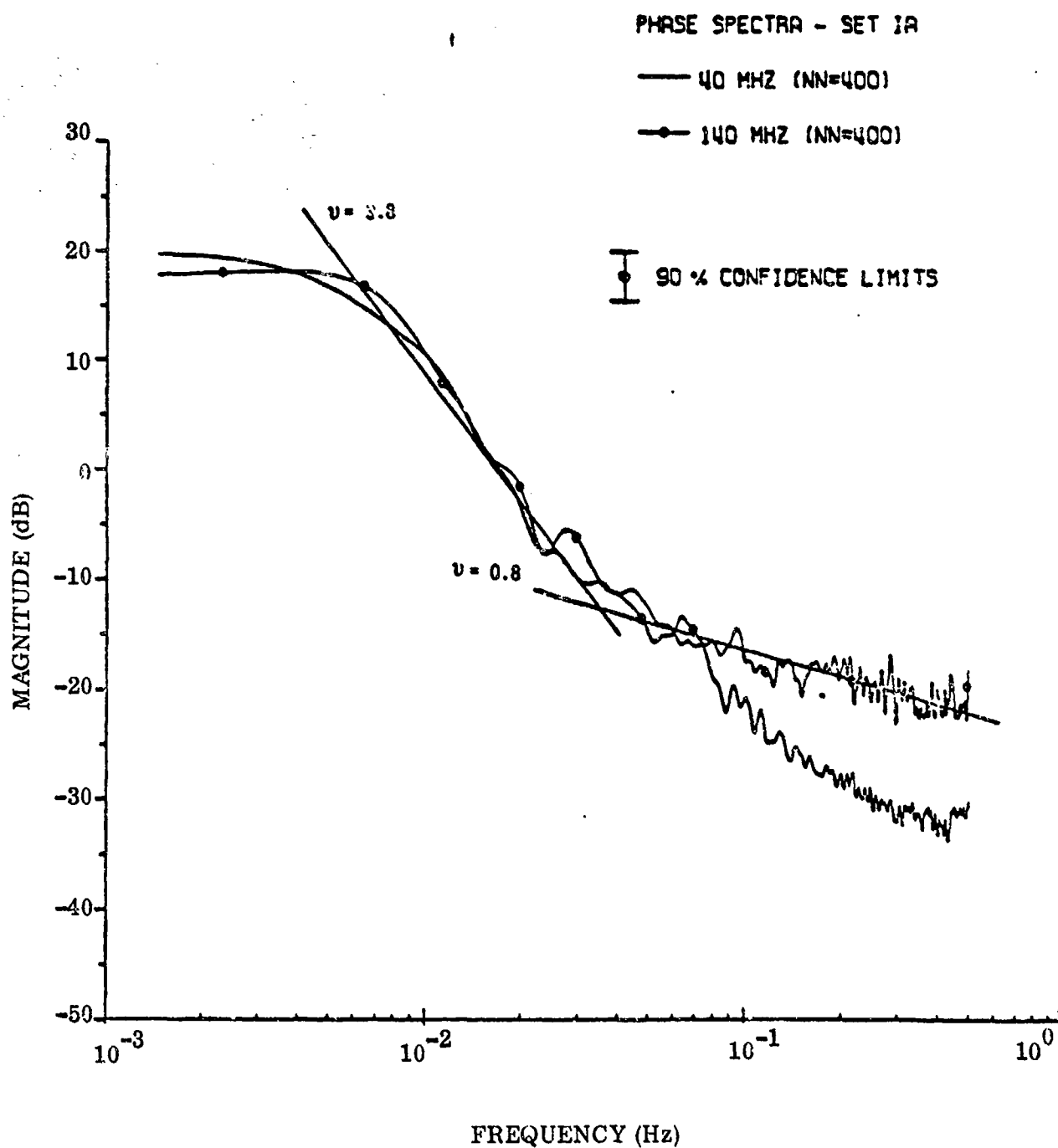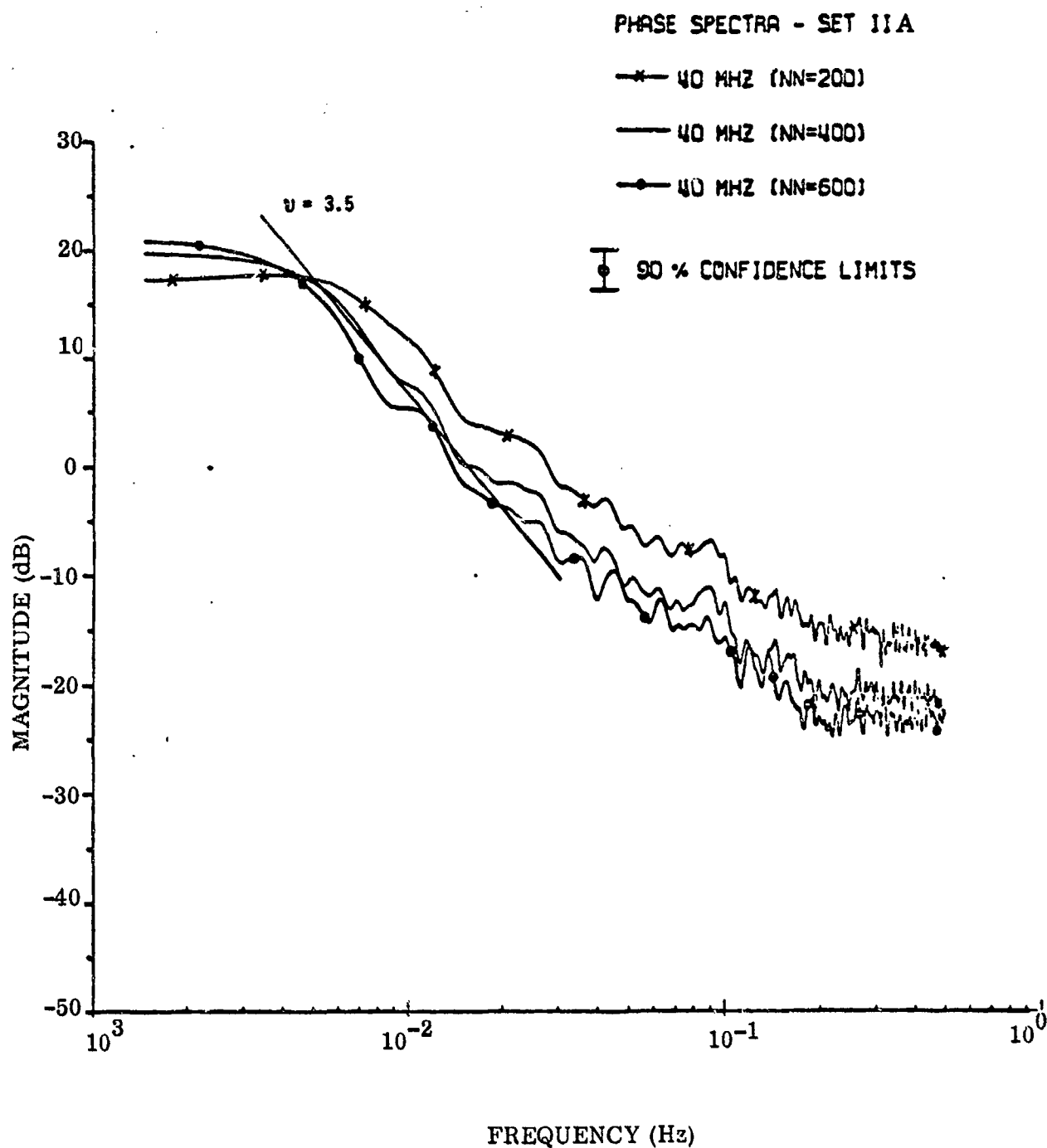
Figure A-10. Superimposed Phase Spectra of 40 and 140 MHz Signals for Set 1A. (After Gjeldum, 1978)
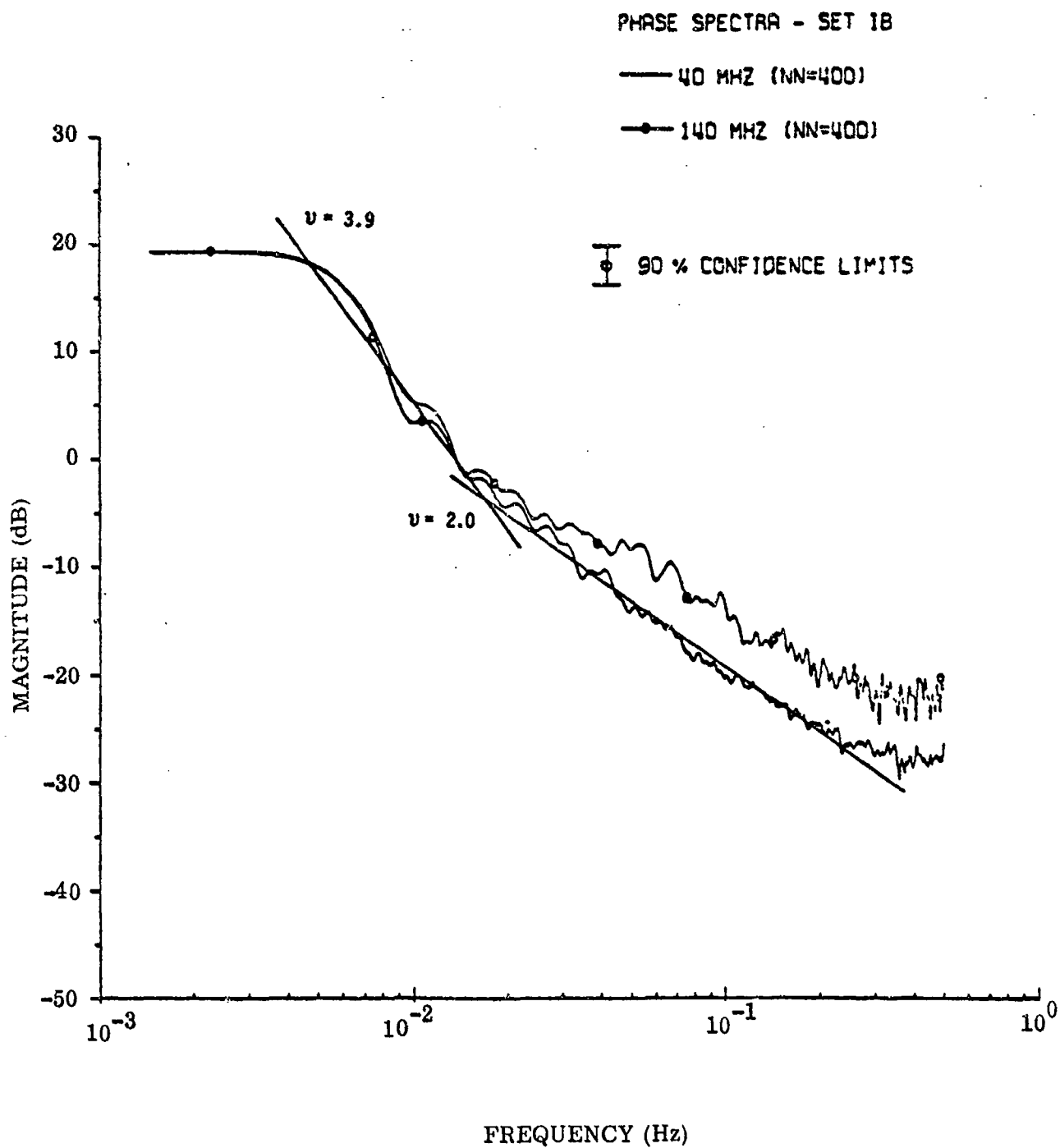
Figure A-11. Superimposed Phase Spectra of 40 and 140 MHz Signals for Set 1B. (After Gjeldum, 1978)

Figure A-12. Superimposed Phase Spectra of 40 MHz Signal for Different
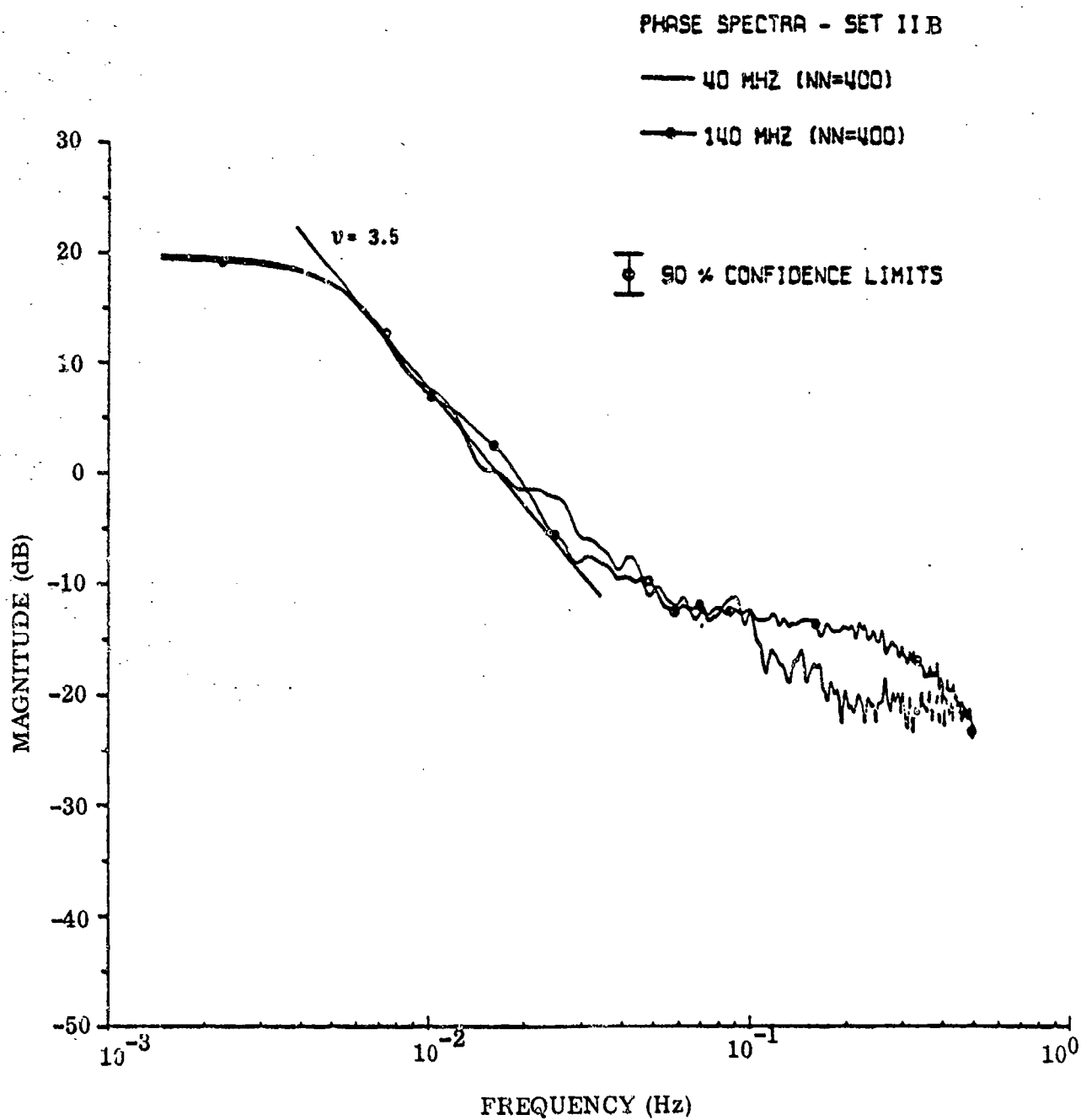Filter Lengths. (After Gjeldum, 1978)

Figure A-13. Superimposed Phase Spectra of 40 and 140 MHz Signals for Set IIB.
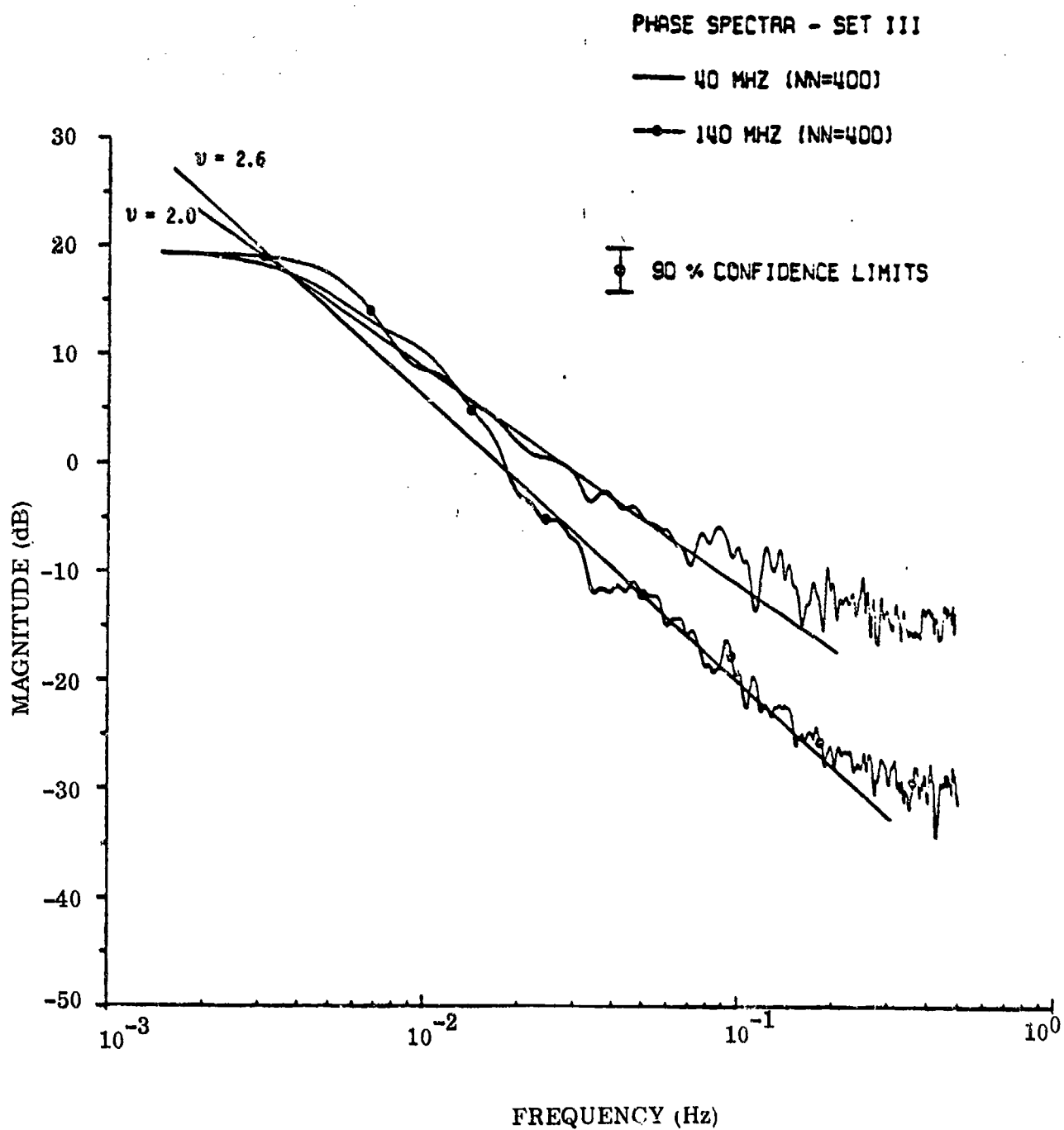(After Gjeldum, 1978)

Figure A-14. Superimposed Phase Spectra of 40 and 140 MHz Signals for Set III.
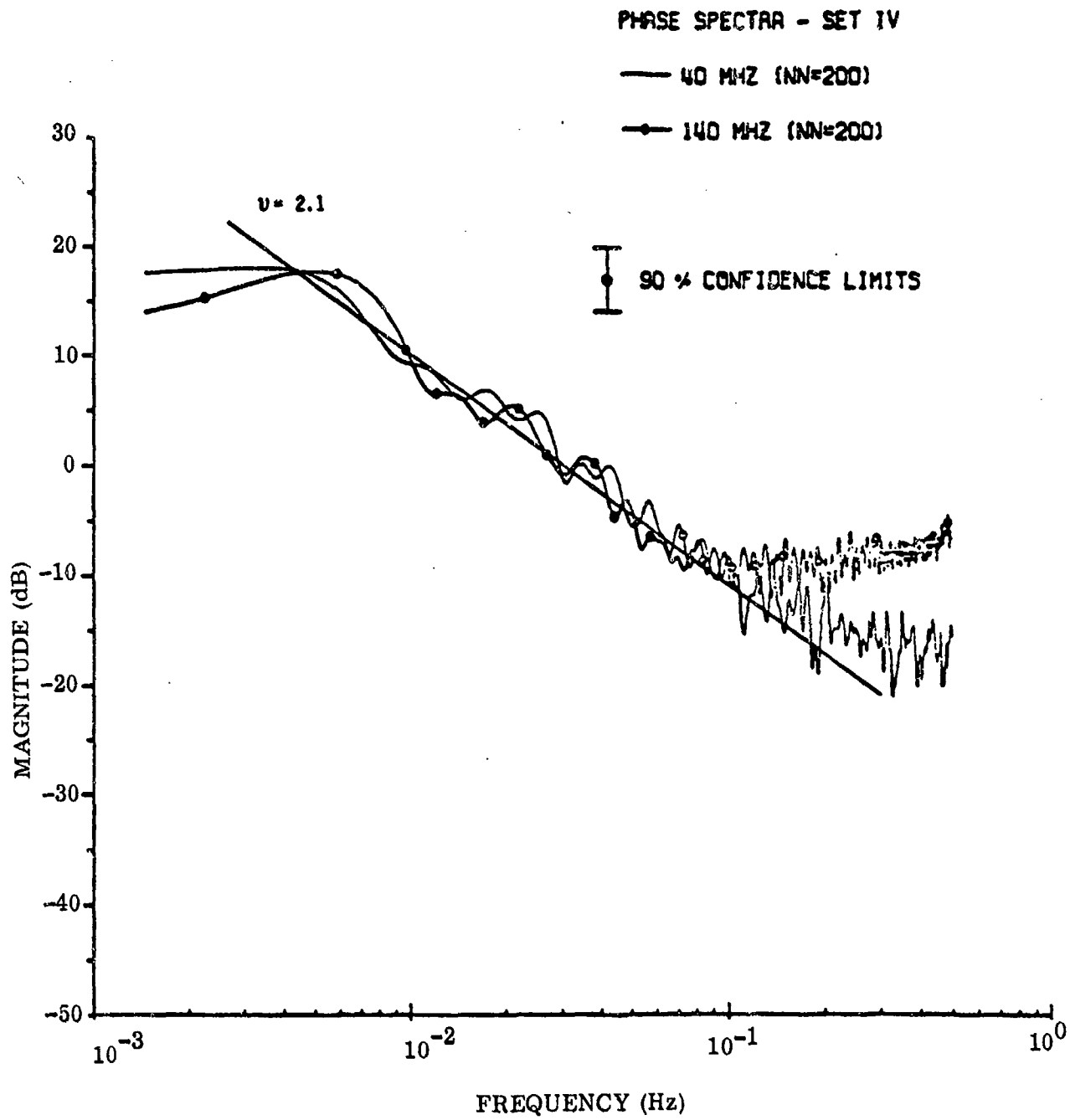(After Gjeldum, 1978)

Figure A-15. Superimposed Phase Spectra of 40 and 140 MHz Signals for Set IV. (After Gjeldum, 1978)